Exceptionally active and stable catalysts for CO_2 reforming of glycerol to syngas

Selin Bac[a], Zafer Say[b,c], Yusuf Kocak[b], Kerem E. Ercan[b], Messaoud Harfouche[d], Emrah Ozensoy[b,e,**], Ahmet K. Avci[a,*]

[a] Department of Chemical Engineering, Bogazici University, Bebek, 34342, Istanbul, Turkey
[b] Bilkent University, Department of Chemistry, 06800, Ankara, Turkey
[c] Department of Physics, Chalmers University of Technology, 412 96, Göteborg, Sweden
[d] Synchrotron-Light for Experimental Science and Applications in the Middle East (SESAME), 19252, Allan, Jordan
[e] UNAM-National Nanotechnology Center, Bilkent University, 06800, Ankara, Turkey

A B S T R A C T

CO_2 reforming of glycerol to syngas was studied on Al_2O_3-ZrO_2-TiO_2 (AZT) supported Rh, Ni and Co catalysts within 600–750 °C and a molar inlet CO_2/glycerol ratio (CO_2/G) of 1–4. Glycerol and CO_2 conversions decreased in the following order: Rh/AZT > Ni/AZT > Co/AZT. Reactant conversions on Rh/AZT exceeded 90% of their thermodynamic counterparts at 750 °C and CO_2/G = 2–4 at which the activity of Ni/AZT was boosted to ~95% of the thermodynamic CO_2 conversion upon increasing the residence time. The loss in CO_2 conversions was below 13% during the 72 h longevity tests confirming the exceptional stability of Rh/AZT and Ni/AZT. However, Co/AZT suffered from sintering, carbon deposition and oxidation of Co sites, demonstrated *via* TEM-EDX, XPS, XANES and *in-situ* FTIR experiments. Characterization of Rh/AZT revealed no significant signs of deactivation. Ni/AZT preserved most of its original metallic pattern and gasified carbonaceous deposits during earlier stages of the reaction.

1. Introduction

The present global energy consumption depends primarily on the utilization of fossil fuels, namely crude oil, coal and natural gas [1]. However, increasing complexity and cost of production and supply of the fossil fuels together with the environmental problems related with their consumption have drawn attention to renewable energy conversion technologies and renewable fuels. In this context, the use of biodiesel as a renewable fuel received notable interest as it can be blended with the refinery diesel and may be used in existing diesel engines without requiring any modifications. These benefits increased the scale of the global biodiesel market from ~8.3×10^4 tons in 2000s [2] to ~3.4×10^7 tons in 2016 [3]. Noticeably, biodiesel production in the US have also increased by > ~15% from 2016 to 2018 [4].

Biodiesel is conventionally synthesized by the trans-esterification of animal-based or vegetable oils in the presence of methanol or ethanol, yielding glycerol as a side product which typically accounts ~10% by mass of the resulting mixture [5,6]. This fraction, however, causes a notable surplus of glycerol when the scale of biodiesel production is

considered. By the year 2020, cumulative global glycerol supply is forecasted to be about 6 times greater than the global glycerol demand (*i.e.* 3×10^6 ton *vs.* 5×10^5 ton, respectively) [5]. Unless valorized into useful products, surplus glycerol will elevate the cost of biodiesel synthesis. Among several options of valorization, catalytic transformation of glycerol to synthesis gas (*i.e.* syngas) receives increasing interest as it contributes to the sustainability of commercially important processes such as Fischer-Tropsch (FT), methanol and dimethyl ether syntheses, all of which start from syngas [7].

Glycerol-to syngas conversion is carried out typically by catalytic steam reforming whose catalysis and reaction engineering aspects are studied extensively and compiled in a number of extensive reviews in the literature [5,8–10]. Steam reforming of hydrocarbons such as natural gas favors syngas with H_2/CO > 2, which is suitable for hydrogen production, but is not aligned with the preferred composition (H_2/CO~1) needed for long-chain hydrocarbon production *via* FT synthesis [11]. The required specification, however, can be obtained by reforming glycerol with CO_2 which can give a theoretical syngas composition of 0.75 [12]. Moreover, glycerol dry reforming (GDR) has a
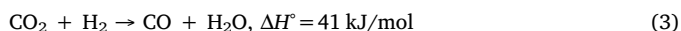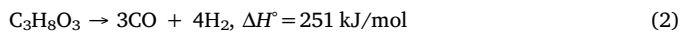
---

* Corresponding author.
** Corresponding author at: Bilkent University, Department of Chemistry, 06800, Ankara, Turkey.
  E-mail addresses: ozensoy@fen.bilkent.edu.tr (E. Ozensoy), avciahme@boun.edu.tr (A.K. Avci).

characteristic benefit of making syngas, a valuable product, through a carbon-negative path, *i.e.* by consuming CO_2 (*i.e.* a greenhouse gas) and glycerol (*i.e.* waste of biodiesel synthesis) according to the following overall reaction:

$$C_3H_8O_3 + CO_2 \rightarrow 4CO + 3H_2 + H_2O, \Delta H° = 292\ kJ/mol \qquad (1)$$
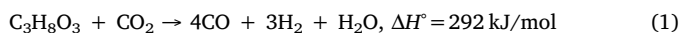
Reaction 1 can be considered as a combination of glycerol decomposition (2) and reverse water gas shift (RWGS, 3), where the latter reaction affects the syngas composition [13]:

$$C_3H_8O_3 \rightarrow 3CO + 4H_2, \Delta H° = 251\ kJ/mol \qquad (2)$$

$$CO_2 + H_2 \rightarrow CO + H_2O, \Delta H° = 41\ kJ/mol \qquad (3)$$

Due to its endothermic nature, GDR is thermodynamically favored at high (> 500 °C) temperatures [13–15] where glycerol can thermally decompose *via* a series of dehydration and dehydrogenation steps yielding hydrocarbons or oxygenates such as methane, ethane, ethylene, acetaldehyde, acrolein, acetone, methanol, ethanol and acetic acid [16]. These molecules may also transform into surface carbon species (C_s) or coke with varying extents depending on the nature of the generated hydrocarbon or oxygenate as well as the catalytic conditions utilized. As presented in Table 1, reforming of the hydrocarbons and gasification of C_s by CO_2 and H_2O (where the last species is produced *in-situ via* RWGS), are other side-reactions that may take place under GDR conditions. It was reported that the extent of coke formation could be reduced with increasing temperatures and become thermodynamically insignificant above 677 °C with $CO_2/G = 1$ [15].

A limited number of theoretical and experimental studies [13–15] exist in the literature focusing on the thermodynamic and catalytic aspects of GDR. Siew et al. [17–20] investigated the effect of La promotion on Ni/Al_2O_3 catalysts under GDR conditions of 650–850 °C and $CO_2/G = 0$–5. It was reported that La promotion improved metal dispersion, decreased carbon deposition and suppressed deactivation. It was also pointed out that CO_2 in the feed stream favored coke gasification. Authors did not quantify the breakdown of CO_2 in GDR, but reported an average glycerol conversion of 90% at 750 °C on the La-promoted catalyst. In another study, Ag-promoted Ni/SiO_2 catalysts were used for GDR [21]. Increasing Ag loading from 0 to 5 wt.% elevated H_2 yield and glycerol conversion (at 700 °C and $CO_2/G = 1$) to ˜27% and ˜33%, respectively. Nevertheless, the promoted catalyst was unable to prevent formation of carbonaceous species during the reaction. The impact of Ag promotion (1, 3 and 5 wt.%) on Al_2O_3 supported Ni catalysts was also studied by the same group at $CO_2/G = 0.5$ and within 600–900 °C and 14.4–72 L/g_{cat}.h [22]. The highest glycerol conversion (40.7%) and H_2 yield (32%) were obtained at 800 °C and 36 L/g_{cat}.h on 3% $Ag-Ni/Al_2O_3$. Although BET specific surface area (SSA) of the catalyst decreased with Ag promotion, high activity of the 3% $Ag-Ni/Al_2O_3$ was attributed to the small metal crystallite size. Despite its high activity, the catalyst was unstable due to the formation of

whisker-type carbonaceous species. Ni-catalyzed GDR was also studied by Lee *et al.* [23,24] who focused on the use of cement clinker (CC: a material composed mainly of CaO and MgO), as the catalyst support. It was reported that carbon formation was reduced upon using CC. Activity tests carried out on the 20% Ni/CC at 750 °C and $CO_2/G = 1.67$ gave glycerol conversions up to ˜80% and $H_2/CO < 2$ [23,24]. Use of CaO supported Ni for GDR was also investigated by Arif *et al.* [25,26] who comparatively studied 15 wt.% Ni loaded CaO, ZrO_2 and La_2O_3 supported catalysts. At 700 °C and $CO_2/G = 1$, the authors reported glycerol conversions of 30%, 20% and 13% on Ni/CaO, Ni/La_2O_3 and Ni/ZrO_2, respectively. Superiority of Ni/CaO was attributed to the improved metal dispersion and smaller NiO crystallite size on CaO [25,26]. Tavanarad et al. [27] studied GDR within 600–750 °C and $CO_2/G = 0$–3, on catalysts supported by mesoporous $\gamma-Al_2O_3$ loaded with different amounts of (5, 10, 15 and 20%) Ni. While 15% Ni loading delivered the best activity, 20 h stability testing showed significant deactivation accompanied by whisker-type carbon formation. Increasing temperature and CO_2/G was found to improve glycerol conversion and decrease H_2/CO which remained always above 1. In an another study, noble metals (Rh, Ru, Ir, Pd and Pt) were impregnated on Al_2O_3 stabilized MgO and the resulting catalysts were tested under GDR conditions of 600–750 °C and $CO_2/G = 0$–3 [28]. BET analysis showed higher SSAs for Rh, Ru and Pd based catalysts, and TEM imaging revealed well-dispersed metal particles with sizes below 5 nm. Activity of noble metals was reported in the decreasing order of Rh > Ru > Ir > Pd > Pt. While up to ˜90% glycerol conversion could be obtained on $Rh/MgO-Al_2O_3$, the catalyst suffered from whisker-type carbon formation and severely deactivated during the 20 h stability test [28].

While the literature provides some information on the catalysis of GDR, a comprehensive molecular-level understanding of the activation and deactivation mechanisms is missing. In addition, there is a lack of data regarding the conversion of CO_2 and comparison of the catalytic performances with the thermodynamic limits. For the first time in the literature, such information was recently provided in detail by Bulutoglu *et al.* [29] for Rh/ZrO_2 and Rh/CeO_2 catalysts. While Rh/ZrO_2 was more active than Rh/CeO_2, the latter turned out to be more stable as verified by the 72 h stability tests and detailed molecular-level *in-situ/ex-situ* spectroscopic/imaging investigations. Activity tests carried out at 600–750 °C and $CO_2/G = 1$–4 showed increasing glycerol and CO_2 conversions. CO_2 conversion was significant only above 700 °C, where increasing temperature led to decreasing coke formation. Even though Rh/ZrO_2 and Rh/CeO_2 gave CO_2 conversions up to ˜23% and ˜16% and glycerol conversions up to ˜77% and ˜72%, respectively, these values remained below their thermodynamic counterparts under all conditions. Therefore, in the current study, we synthesized Rh, Ni and Co-based catalysts supported on a ternary oxide, $Al_2O_3-ZrO_2-TiO_2$ (AZT) with the aim of developing stable and active catalysts that can run near the thermodynamic limits of GDR. We also carried out activity tests at 600–750 °C and $CO_2/G = 1$–4 together with 72 h time-on-stream (TOS) stability experiments. AZT presents itself as a promising support material suitable to cope with the harsh operational environment of GDR, particularly due to its high SSA (> 100 m²g⁻¹) [30] favoring fine metal dispersion, high activity and high coking resistance. Furthermore, superior activity and stability of Rh in dry reforming of hydrocarbons [31–35] inspired us to use it as a benchmark precious metal catalyst for the cheaper, yet promising alternatives, such as Ni and Co. For the first time in the literature, we report superior Rh/AZT and Ni/AZT catalysts both of which can deliver > 90% of the thermodynamic CO_2 and glycerol conversions with negligible activity loss. These catalysts clearly outperform the existing Rh- and Ni-based catalysts previously reported in the literature [17–29]. In the current work, in addition to activity and stability tests, AZT supported Rh, Ni and Co catalysts were also characterized before and after GDR reaction by means of *in-situ/ex-situ* spectroscopic/imaging techniques to provide valuable insights regarding the molecular-level origins of catalytic

Table 1
Reactions of steam and dry (CO_2) reforming of methane, ethane and ethylene (representative hydrocarbons) and coke gasification.

Reaction	$\Delta H°$ (kJ/mol)	Reaction number
Steam reforming reactions		
$CH_4 + H_2O \rightarrow CO + 3H_2$	206	(4)
$C_2H_6 + 2H_2O \rightarrow 2CO + 5H_2$	346	(5)
$C_2H_4 + 2H_2O \rightarrow 2CO + 4H_2$	210	(6)
Dry reforming reactions		
$CH_4 + CO_2 \rightarrow 2CO + 2H_2$	247	(7)
$C_2H_6 + 2CO_2 \rightarrow 4CO + 3H_2$	430	(8)
$C_2H_4 + 2CO_2 \rightarrow 4CO + 2H_2$	292	(9)
Surface carbon gasification reactions		
$C_s + H_2O \rightarrow CO + H_2$	131	(10)
$C_s + 2H_2O \rightarrow CO_2 + 2H_2$	90	(11)
$C_s + CO_2 \rightarrow 2CO$	172	(12)

activity and stability.

2. Experimental

2.1. Catalyst synthesis

The ternary oxide AZT support with the mass composition of $Al_2O_3:ZrO_2:TiO_2 = 50:35:15$ was prepared by the conventional sol-gel technique which involved dissolving zirconium isopropoxide (Sigma Aldrich, ACS Reagent, 70 wt.% in 1-propanol), titanium (IV) isopropoxide (Sigma Aldrich, ACS Reagent, 97%) and aluminum sec-butoxide (Sigma Aldrich, ACS Reagent, 97%) in 100 ml of 2-propanol (Sigma Aldrich, ACS Reagent > 99.5%) [30]. The slurry was then stirred for 60 min under ambient conditions, followed by drop-wise addition of 9 ml of 0.5 M nitric acid solution (Sigma Aldrich, ACS Reagent, 65%) in order to obtain a gel which was dried under ambient conditions for 2 days and calcined at 750 °C under air. Catalysts used in this study, namely, 1 wt.% Rh/AZT, 5 wt.% Ni/AZT and 5 wt.% Co/AZT, were prepared by conventional incipient wetness impregnation method. Rh loading is kept at 1 wt.% as it is a widely used value for the Rh-based catalysts utilized in hydrocarbon reforming reactions [28,36] carried out under conditions similar to those employed in the present study and allows direct comparison with the GDR performance of Rh/ZrO_2 and Rh/CeO_2 catalysts tested previously [29]. Ni loading was chosen to be 5 wt.%, as this was the optimum loading among 1, 5 and 10 wt.% Ni/AZT catalysts in terms of catalytic performance (data not shown). Ni loadings greater than 5 wt.% was found to have adverse effects on metal dispersion [37]. Being a non-noble metal like Ni, Co was loaded on AZT with an identical loading (i.e. 5 wt.%) simply for the ease of comparison.

In order to obtain 1.0 g of active Rh/AZT catalyst, 7.1×10^{-2} ml of liquid Rh-precursor ($Rh(NO_3)_3$, purity: 10% (w/w) Rh in > 5 wt.% HNO_3 solution, Sigma-Aldrich) was dissolved in deionized water. The aqueous precursor solution was drop-wise added onto the ternary oxide support by means of a peristaltic pump under vacuum. The resulting slurry was dried overnight in an oven at 110 °C and then calcined in a muffle furnace at 800 °C for 4 h. An identical protocol was used for the syntheses of Ni/AZT and Co/AZT. A necessary amount of (2.5×10^{-1} g/ g catalyst) $Ni(NO_3)_2.6H_2O$ (Sigma Aldrich, ≥97.0%) or $Co(NO_3)_2.6H_2O$ (Sigma Aldrich, ACS Reagent, ≥99.0%) was dissolved in deionized water and impregnated onto the AZT support. Resulting slurries were dried overnight at 110 °C followed by calcination at 800 °C for 4 h. Prior to the reaction tests, the catalysts were in-situ reduced at 800 °C for 2 h under 40 Nml/min H_2 (purity > 99.99%, Linde GmbH) flow [20,23,36].

2.2. Catalyst characterization

2.2.1. N_2 physisorption

BET isotherms were obtained by using a Quantachrome Nova 2200e automated gas adsorption system with liquid nitrogen at a temperature of −196 °C. SSAs of the fresh (i.e. reduced) and spent Rh/AZT, Ni/AZT and Co/AZT catalysts (after 5 h reactions at 750 °C, $CO_2/G = 4$, residence time = 3.75 mg$_{cat}$.min/Nml), and of the pure support material (AZT) were measured by means of multi-point BET analysis.

2.2.2. Transmission electron microscopy (TEM) and energy dispersive X-Ray spectroscopy (EDX)

TEM imaging and EDX analysis of the fresh (i.e. reduced) and spent catalysts (after 5 h and 72 h reactions at 750 °C, $CO_2/G = 4$, residence time = 3.75 mg$_{cat}$.min/Nml) were performed via a FEI, Tecnai G2 F30 microscope using an electron beam voltage of 300 kV. Before TEM-EDX analysis, each sample was dispersed in ethanol and sonicated for 5 min. Then, the sample suspension was transferred on a copper TEM grid by using a micropipette. The excess solution was removed, and the copper grid was dried in the fume hood at room temperature overnight. While

bright-field imaging mode was used for the high resolution TEM (HR-TEM) measurements, high angle annular dark field scanning transmission electron microscopy (HAADF-STEM) was utilized for the EDX analysis.

2.2.3. X-ray photoelectron spectroscopy (XPS)

XPS characterization studies were performed on fresh (i.e. reduced) and spent catalysts (after 5 h and 72 h reactions at 750 °C, $CO_2/G = 4$, residence time = 3.75 mg$_{cat}$.min/Nml) by using a SPECS PHOIBOS hemispherical energy analyzer. A monochromatic Al-Kα X-ray excitation source (15 kV, 400 W) and an electron flood gun were employed during the XPS data acquisition.

2.2.4. In-situ FTIR spectroscopy

In-situ FTIR spectroscopic experiments were carried out in transmission mode using a custom-design batch type stainless steel reactor attached to Bruker Tensor 27 spectrometer whose details have been described elsewhere [38,39]. FTIR spectra were collected at 323 K by averaging 32 scans with a spectral resolution of 4 cm^{-1}. Each catalyst was finely ground prior to pressing onto a lithographically etched W-grid sample holder. Corresponding in-situ CO(g) adsorption analyses were performed by exposing the fresh and spent catalyst surfaces to 10.0 Torr of CO(g) for 10 min at 50 °C. Prior to analysis of materials, reactor chamber was evacuated to ˜10^{-2} Torr at 127 °C for 60 min to acquire a background spectrum for each catalyst in the vacuum.

2.2.5. X-ray absorption near-edge spectroscopy (XANES)

Ex-situ XANES data were collected at the XAFS/XRF beamline of SESAME (Synchrotron-Light for Experimental Science and Applications in the Middle East, Allan, Jordan). XANES experiments were performed in transmission mode for Co and Ni metallic foils and for CoO, Co(acac) and $Ni(NO_3)_2$ refence samples. Due to the relatively low concentration of Ni and Co in the Ni/AZT and Co/AZT catalysts, these samples were analyzed in fluorescence mode. Rh edges of the Rh/AZT samples cannot be analyzed due to the energy range limitations of the Si < 111 > crystal of the monochromator utilized at this beamline. For Co and Ni K-edges, 3 successive (repeated) spectra was acquired for each sample in order to enhance the signal to noise ratio (S/N). Edge energy (E_0) values in the XANES data were chosen as the energies where the second derivatives of the corresponding spectra vanishes (i.e. inflection points). Analysis (normalization, merging, etc.) of the XANES data was carried out using Athena part of the Demeter software package [40].

2.3. Catalytic performance experiments

The experiments were conducted in a down-flow quartz tubular packed bed reactor placed inside a three-zone furnace (Protherm PZF 12/50/500). The catalyst bed, whose position at the center of the quartz tube overlapped with the center of the second zone of the furnace, was consisted of physical mixture of 20 mg active catalyst (Rh/AZT, Ni/AZT or Co/AZT) with 700 mg diluent α-Al_2O_3. The catalyst-diluent mixture was supported by a quartz wool plug. Flow of liquid glycerol (Sigma-Aldrich, purity: 99.5%) was controlled by a Shimadzu LC-20AD HPLC pump and set to deliver 4 Nml/min of glycerol upon its evaporation in all experiments. Inlet flow of CO_2 (purity > 99.99%, Linde GmbH) was determined according to the assigned CO_2/G ratio and the balance gas N_2 (purity > 99.99%, Linde GmbH) flow rate was adjusted to obtain a constant total flow rate of 40 Nml/min. Precise dosing of CO_2, N_2 and H_2 (purity > 99.999%, Linde GmbH), the reduction gas, was carried out via Brooks 5850E Series Mass Flow Controllers. Geometric and operational details regarding mixing, evaporation and injection of the glycerol-CO_2-N_2 mixture can be found elsewhere [29]. Condensable species (i.e. water, unconverted glycerol and any other possible side products in liquid phase) in the product mixture were knocked out inside two serially-connected cold traps

before transferring the reactor effluent to multiple on-line gas chromatograph (GC) units. The first GC, Shimadzu GC-2014, was consisted of a 60–80 mesh size Molecular Sieve 5A packed column and was used to detect and quantify H_2, N_2, CH_4 and CO *via* a thermal conductivity detector (TCD) in the presence of Ar (purity > 99.99%, Linde GmbH) as the carrier gas. The second GC, Agilent 6850 N, consisting of TCD and 80–100 mesh size Porapak Q packed column run with He carrier gas (purity > 99.99%, Linde GmbH) was used to analyze N_2, CO_2, CH_4, C_2H_4 and C_2H_6. GC units were connected in parallel configuration and each of them was equipped with six-way sampling valves that involved sample loops of 1 ml volume. Further details regarding the product analysis units and the schematic presentation of the experimental set-up can be found in [29].

Catalytic experiments involved investigation of the effects of reaction temperature (T = 600–750 °C), CO_2/G ratio (1–4) and residence time (0.5–3.75 mg_{cat}.min/Nml) on CO_2 and glycerol conversions, product distribution and syngas composition. Residence time was defined as the ratio of the mass of catalyst to the total inlet volumetric flow rate, which was kept constant at 40 Nml/min in all experiments. While studying the impact of a particular parameter, other parameters were kept constant at their default values, namely 750 °C, CO_2/G = 4 and 0.5 mg_{cat}.min/Nml which corresponded to packing of 20 mg of catalyst. Duration of the catalytic activity tests was fixed at 5 h. The first data was taken 0.5 h after the onset of the experiment, while the rest were collected every following 45 min. The reaction system typically reached steady-state conditions in the second hour of the experiments. Thus, the first two data points collected at 30th and 75th min were discarded while reporting reactant conversions and product yields. The 72 h TOS stability runs as well as experiments for producing catalyst samples for characterization studies were carried out at a longer residence time of 3.75 mg_{cat}.min/Nml (*i.e.* on 150 mg of catalysts without dilution) in an attempt to augment the extent of possible deactivation phenomena such as sintering and coke deposition. CO_2 conversion (X_{CO_2}), glycerol conversion to gaseous products (X_G) and product yields (Y_i) were used as the metrics to monitor catalytic activity [29]:

$$X_{CO_2}(\%) = \frac{F_{CO_2,in} - F_{CO_2}}{F_{CO_2,in}} \times 100 \tag{13}$$

$$X_G(\%) = \frac{2F_{H_2} + 4F_{CH_4} + 4F_{C_2H_4} + 6F_{C_2H_6}}{8F_{G,in}} \times 100 \tag{14}$$

$$Y_i = \frac{F_i}{F_{G,in}} \tag{15}$$

In Eqs. (13–15) $F_{i,in}$ (mol/min) refer to the molar flow rate of species i in the feed stream (*i.e.* CO_2 and gaseous glycerol) and F_i (mol/min) represents the outlet molar flow rate of the gaseous products (*i.e.* CO, H_2, CH_4, C_2H_4 and C_2H_6). Glycerol conversion (Eq. 14) was formulated by elemental hydrogen balance that included all detectable hydrogen-containing species in the gas phase. H_2O, which is the product of RWGS and reverse of possible side reactions 4–6, 10 and 11 (Table 1), was not detected and quantified. Thus, it was not included in Eq. (14). As discussed in detail by Bulutoglu et al. [29] the impact of the lack of H_2O in hydrogen balance on glycerol conversions remained negligible. Moreover, the common use of Eq. (14) in the existing GDR studies [17–26] allowed direct comparison of the present results with the glycerol conversions reported in the literature. The results reported in the present study were found to be reproducible in all cases, as the difference between the performance metrics (X_{CO_2}, X_G and Y_i) of successive experiments remained below 1%.

In order to quantify possible involvement of the AZT support, diluent and quartz wool, a series of blank experiments were conducted. In the first group of blank experiments, the packed zone of the reactor tube involved only α-Al_2O_3 and quartz wool, and tested in all parametric combinations. None of those materials showed activity. While no CO_2 conversion was noted, thermally induced conversion of glycerol was

Table 2
SSAs of the AZT support material and the catalysts.

Catalyst	SSA (m^2/g)	
	Fresh	Spent (5h)
AZT	182	–
Rh/AZT	134.7	128.4
Ni/AZT	142.9	139.8
Co/AZT	113.1	112.6

observed. The second group of blank experiments aimed to capture any possible contribution of AZT on CO_2 conversion, and involved addition of 20 mg of AZT to the diluent and testing at 700–750 °C and CO_2/G = 1–4. As CO_2 conversion is thermodynamically favored only above 700 °C [29], no blank tests were conducted in the 600–700 °C range. The blank tests were continued by means of packing 150 mg AZT to provide further insight into the possible role of AZT on CO_2 conversion. Outcomes of the blank tests involving AZT are reported in Section 3.2.

3. Results and discussion

3.1. Structural and functional characterization studies

3.1.1. Surface area and porosity measurements

SSA data obtained by N_2 physisorption on the fresh (*i.e.* reduced) and 5 h-spent catalysts (after reaction at 750 °C, CO_2/G = 4, residence time = 3.75 mg_{cat}.min/Nml) are presented in Table 2. As expected, impregnation of the metals on the AZT support decreased SSA due to the blockage of the pores. The same effect was also observed in the total pore volumes of the AZT support and of the fresh Rh/AZT, Ni/AZT and Co/AZT catalysts which were measured as 2.53×10^{-1}, 2.17×10^{-1}, 1.6×10^{-1} and 1.57×10^{-1} ml/g, respectively. The results also show that SSA of the fresh Co/AZT sample was notably smaller than those of the fresh Rh/AZT and Ni/AZT samples. This finding was well aligned with (i) the comparative TEM-EDX analyses of the fresh samples (Section 3.1.2) that pointed out Co/AZT as the catalyst with the biggest average metal cluster size of *ca.* 40–50 nm covering the biggest portion of the AZT surface and (ii) the catalytic activity experiments in which Co/AZT delivered the lowest conversions of glycerol and CO_2 (Sections 3.2.1 and 3.2.2). It is worth mentioning that all of the catalysts had limited (*i.e.* < 5%) loss in their SSA upon their 5 h exposure to reaction conditions that involved the highest temperature (750 °C) and CO_2/G (4). This finding was correlated with the improved thermal stability of AZT reported in the literature [30]. Average pore diameter of the AZT support was measured as 5.06×10^{-9} m.

3.1.2. TEM and EDX measurements

Structural properties of the Rh/AZT (Fig. 1), Ni/AZT (Fig. 2) and Co/AZT (Figs. 3 and 4) catalysts were investigated in their fresh forms before the GDR reaction, as well as after 5 h and 72 h GDR reaction tests using TEM and EDX techniques. It can be seen in Fig. 1 that the average Rh particle size of the fresh Rh/AZT sample was *ca.* 3–4 nm (Fig. 1a and b) which did not change significantly neither after 5 h (Fig. 1d and e) nor after 72 h (Fig. 1f) GDR reaction tests. It is also important to note that Rh particle size distribution was quite narrow without large variations or heterogeneity in particle sizes. Presence of Al, Zr, Ti and Rh in the fresh Rh/AZT catalyst composition was also verified *via* EDX as shown in Fig. 1c.

Fig. 2 shows similar studies on the Ni/AZT catalyst. Fig. 2a and b reveal the nature of the fresh Ni/AZT catalyst exhibiting an average Ni particle size of *ca.* 10–15 nm. However, in contrast to the relatively monodisperse Rh particles on Rh/AZT (Fig. 1), Ni particles on the Ni/AZT surface showed a larger variation in their particle sizes. EDX data in Fig. 2c confirms the presence of Ni, Al, Zr and Ti in the fresh Ni/AZT catalyst composition. Fig. 2d and e show the surface of the Ni/AZT
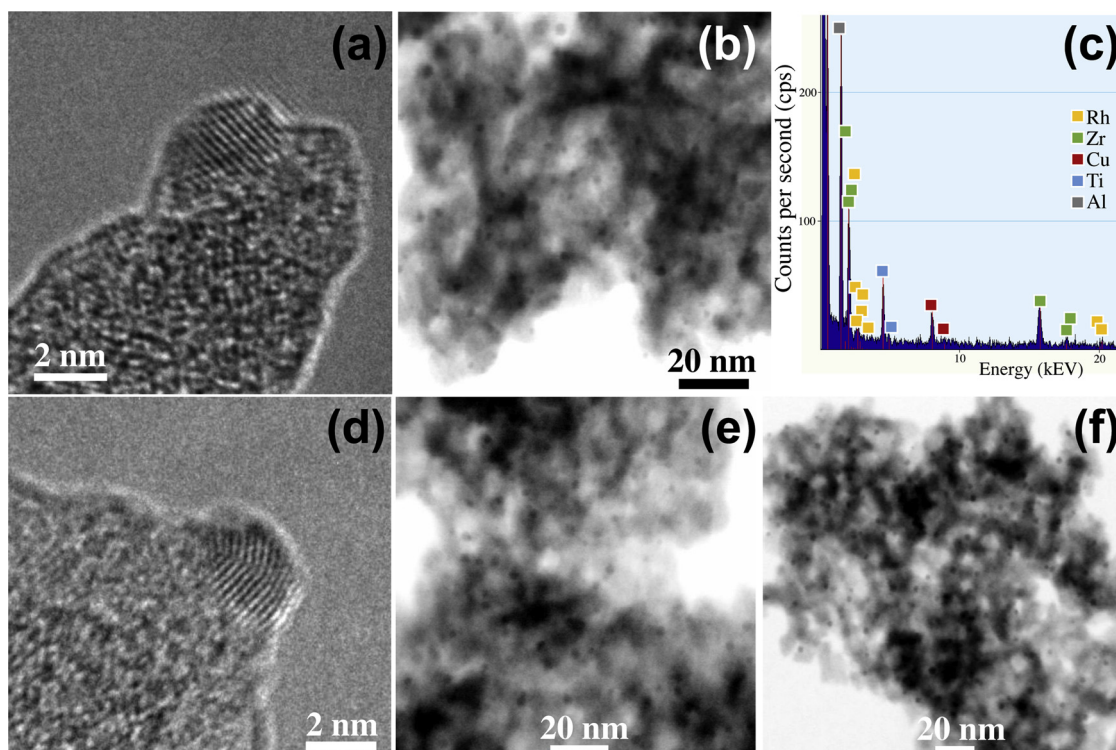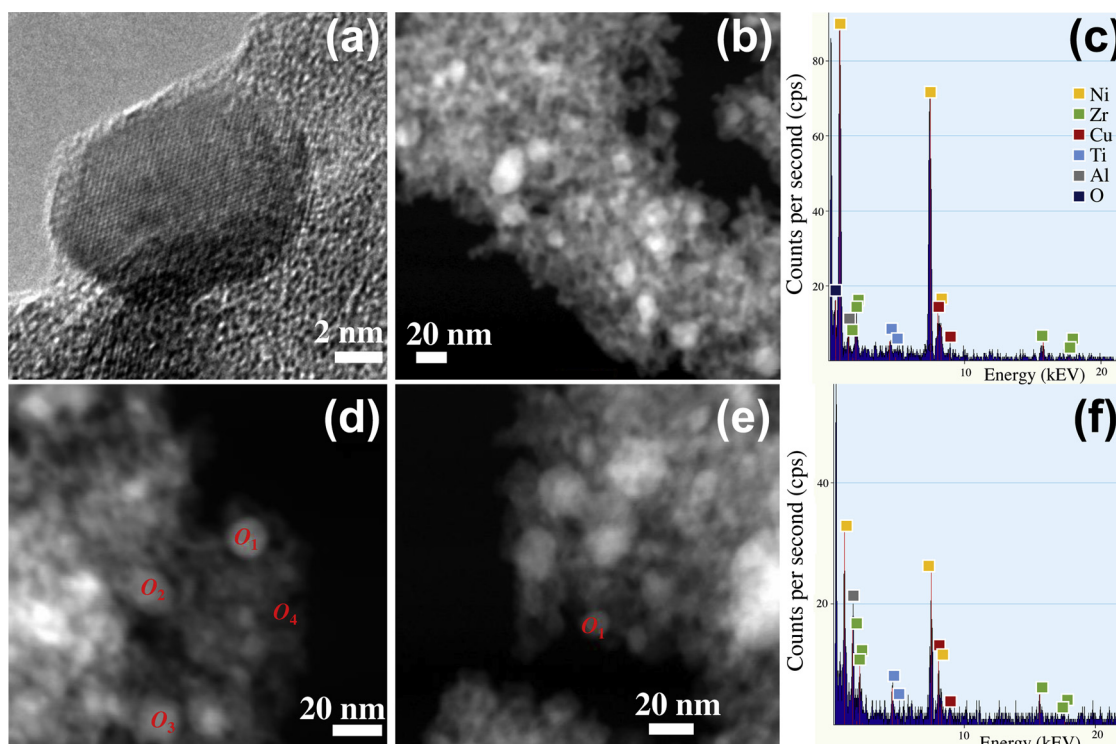
Fig. 1. (a) HR-TEM and (b) HAADF images of fresh Rh/AZT catalyst. (c) A representative EDX spectrum for the fresh Rh/AZT catalyst. (d) HR-TEM and (e) HAADF images of Rh/AZT catalyst after a 5 h GDR reaction test. (f) HAADF images of Rh/AZT catalyst after a 72 h GDR stability test (conditions for spent catalyst: T = 750 °C, CO_2/G = 4, residence time = 3.75 mg_{cat}.min/Nml).

Fig. 2. (a) HR-TEM and (b) HAADF images of fresh Ni/AZT catalyst. (c) A representative EDX spectrum for the fresh Ni/AZT catalyst. (d) HAADF image of Ni/AZT catalyst after a 5 h GDR reaction test. (e) HAADF image of Ni/AZT catalyst after a 72 h GDR stability test. (f) EDX spectrum obtained from the point labeled as "O_1" in (e) (conditions for spent catalyst: T = 750 °C, CO_2/G = 4, residence time = 3.75 mg_{cat}.min/Nml).
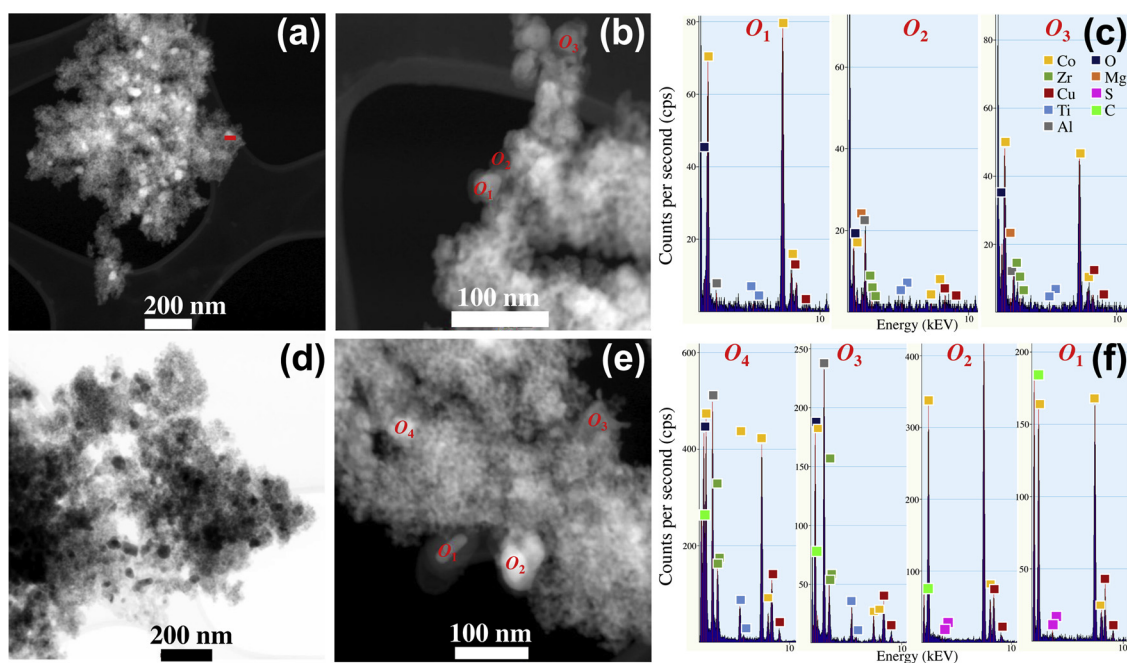
Fig. 3. (a–b) HAADF images of fresh Co/AZT catalyst, (c) EDX spectra obtained from the points labeled as "O_1, O_2, O_3" in (b). (d) TEM image of Co/AZT catalyst after a 5 h GDR reaction test. (e) HAADF image of Co/AZT catalyst after a 72 h GDR stability test. (f) EDX spectra obtained from the points labeled as "O_1, O_2, O_3, O_4" in (d) (conditions for spent catalyst: T = 750 °C, CO_2/G = 4, residence time = 3.75 mg_{cat}.min/Nml).
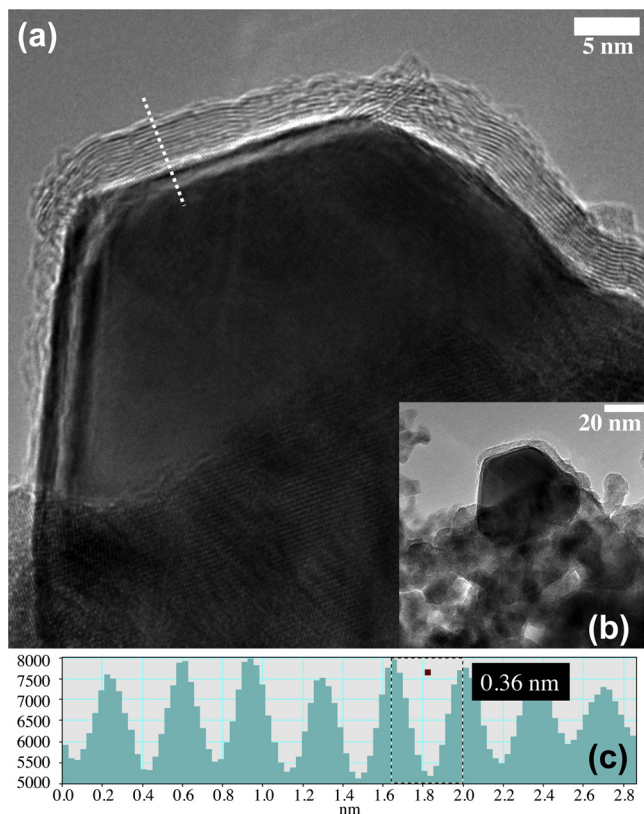

Fig. 4. (a) HR-TEM and (b) TEM images of Co/AZT catalyst after a 72 h GDR stability test. (c) Distance between lattice across the surface coke overlayer (emphasized with the white dashed line) shown in (a) (conditions for spent catalyst: T = 750 °C, CO_2/G = 4, residence time = 3.75 mg_{cat}.min/Nml).

catalyst after 5 h and 72 h GDR reaction tests, respectively. Points labeled as O_1-O_4 in Fig. 2d (corresponding to 5 h-spent Ni/AZT catalyst) were investigated with EDX (data not shown). Fig. 2f illustrates the EDX

data corresponding to a Ni particle (labeled as O_1) on the Ni/AZT system after 72 h GDR test, where Ni particles can be readily identified *via* TEM-EDX. Due to the heterogeneity of the Ni particle sizes on Ni/AZT, it is difficult to conclusively distinguish the changes in average Ni particle size before and after 5 h and 72 h GDR reaction tests *via* TEM. Nevertheless, it can be argued that the changes in Ni particle size after GDR reaction are minor.

Co/AZT sample was also analyzed *via* TEM-EDX as presented in Fig. 3. Average Co particle size on fresh Co/AZT catalyst was *ca.* 40–50 nm (Fig. 3a and b) which was much greater than the corresponding average particle size values for Rh/AZT and Ni/AZT. Furthermore, Fig. 3b indicates that some of the Co particles may be embedded/covered/encapsulated by the AZT support. This is particularly evident for the Co particles labeled as O_1 and O_3 in Fig. 3b, where the presence of Co at these locations were further verified *via* EDX as shown in Fig. 3c. TEM images obtained after 5 h and 72 h GDR reaction tests (Fig. 3d and e, respectively) indicate that Co particles further grew in size after the GDR reaction. In certain cases, Co crystals (*e.g.* Co particle labeled as O_1 in Fig. 3e, whose Co content was confirmed in Fig. 3f *via* EDX), adopted even elongated ordered shapes such as rod-like features.

A detailed analysis of the Co/AZT catalyst after 72 h GDR reaction yielded further valuable information regarding the catalytic poisoning phenomena (Fig. 4). As can be seen in Fig. 4a and b, when the Co/AZT system was exposed to GDR reaction conditions for an extended duration of time (*i.e.* 72 h), a readily visible overlayer film covered the truncated cubooctahedral-shaped Co active sites. Nature of this passivation film can be understood by examining the interlayer distances inside the film. Interlayer spacing of the passivation film was measured to be 0.36 nm (Fig. 3c), which is consistent with the typical interlayer distance in graphite/graphite oxide structures [41]. Thus, it is clear that the Co active sites on the Co/AZT catalyst surface suffered from severe coke formation after 72 h GDR reaction. Note that, such a clearly discernible coke formation was not detectable in the TEM analysis of the Rh/AZT and Ni/AZT samples after 5 h and 72 h GDR reaction tests (Figs. 1 and 2). As will be discussed in later sections, these observations are also in good accordance with the current XPS measurements which indicated the presence of significantly larger amounts of coke deposition on the Co/AZT catalyst after the GDR reaction tests, while surface

Table 3
Surface atomic composition (% by weight) values of the fresh, 5 h and 72 h spent catalysts obtained *via* XPS (conditions for spent catalysts: T = 750 °C, CO_2/G = 4, residence time = 3.75 mg$_{cat}$.min/Nml).

		Fresh	Spent (5h)	Spent (72h)
Rh/AZT	C1s	19.1	19.5	18.2
	Rh3d	0.3	0.4	0.3
Ni/AZT	C1s	30.4	44.3	31.8
	Ni2p	0.4	0.5	0.4
Co/AZT	C1s	16.7	34.1	33.3
	Co2p	1.5	1.5	1.1

carbon (C_s) level for the spent Rh/AZT catalyst was almost identical to its fresh counterpart and Ni/AZT catalyst increased its C_s content only in a slight manner.

3.1.3. XPS measurements

XPS measurements were carried out in order to obtain information about the surface chemistry and surface composition of the fresh Rh/AZT, Ni/AZT and Co/AZT catalysts and after 5 h and 72 h GDR reaction tests. Table 3 presents the surface atomic composition data for these catalysts obtained *via* XPS. In terms of the relative surface concentrations of the active sites, it is apparent that Co/AZT has a significantly higher active site (Co) surface concentration as compared to that of Rh and Ni, both of which have comparable surface active site concentrations. This is rather interesting because, as will be shown in the forthcoming sections, Co/AZT is significantly less active in GDR reaction than Rh/AZT and Ni/AZT. Discrepancy between the activity and surface site concentration can be explained in the light of the current TEM data suggesting that average particle size of Co on Co/AZT is 40–50 nm in contrast to Rh (3–4 nm) on Rh/AZT and Ni (10–15 nm) on Ni/AZT. In other words, due to the smaller surface-to-volume ratio of Co nanoparticles, most of the Co atoms in the large Co clusters are not accessible by the reactants during the GDR reaction.

Additional valuable information can also be acquired by following the C_s content of the Rh/AZT, Ni/AZT and Co/AZT catalysts before and after GDR reaction as shown in Table 3. Firstly, it is seen that C_s contents of the fresh Rh/AZT and Co/AZT catalysts are comparable, while fresh Ni/AZT reveals a much greater C_s content. During the synthesis of the catalysts, nitrate salts of Rh, Co and Ni were used. Hence, it is unlikely that the source of the observed C_s on fresh catalysts are associated with Rh, Ni or Co precursors. On the other hand, the sol-gel synthetic protocol used in the synthesis of AZT support (Section 2.1) contained significant amounts of carbonaceous species. Owing to the fact that Rh and Co are relatively more efficient combustion/oxidation catalysts than Ni, greater extents of carbonaceous species could be removed during the calcination of Rh/AZT and Co/AZT catalysts in air *via* combustion in atmospheric oxygen, leading to the detection of significantly lower initial C_s contents on the fresh Rh/AZT and Co/AZT samples as compared to Ni/AZT.

Evolutions of the C_s content on the 5 h and 72 h spent catalyst samples are also presented in Table 3. It is clear that the C_s content of

the Rh catalyst was identical before and after 5 h and 72 h GDR reactions. This striking finding implies that Rh/AZT had excellent resistance against coking during GDR. For the Ni/AZT catalyst, C_s content noticeably increased in the first 5 h of the GDR reaction. However, upon extending exposure to GDR for 72 h, C_s content on Ni/AZT is found to diminish and approach to that of its fresh counterpart. In other words, significant amount of coking present over Ni/AZT surface in the first 5 h of the GDR reaction could be removed by probably gasification reactions on Ni sites, providing a long-term stability for Ni/AZT catalyst and long-term tolerance against coking. Note that C_s content of Ni/AZT after 72 h GDR test was still somewhat greater than that of the fresh Ni/AZT. In stark contrast to Rh/AZT and Ni/AZT, C_s content of Co/AZT increased by more than 100% in the first 5 h of the GDR reaction and this value remained invariant after 72 h of GDR reaction. Hence, it is apparent that extent of coking of Co/AZT under GDR reaction conditions was drastically more severe and also irreversible as compared to that of Rh/AZT and Ni/AZT. This observation is in very good agreement with the current TEM data for Co/AZT revealing the presence of a thick graphite/graphite oxide (coke) passivation film on the surface of the Co nanoparticles of the Co/AZT catalyst after 72 h GDR reaction (Fig. 4).

Fig. 5a shows the Rh3d region of the XPS data for fresh Rh/AZT catalysts as well as its spent counterparts used in 5 h and 72 h GDR experiments. For all of these catalysts, three different Rh3d$_{5/2}$ features are detectable located at 307.4, 308.8 and 310.5 eV, which can be ascribed to Rh^0, Rh$^+$ and Rh^{3+} species, respectively [42]. These observations are also consistent with the presence of unique surface acid sites observed on the Rh/AZT catalyst that are different than that of the AZT support material which were detected *via in-situ* FTIR spectroscopic investigation of pyridine adsorption (Fig. S1), as well as the presence of additional low-temperature H_2-consumption (*i.e.* reduction) features observed in the temperature programmed reduction (TPR) analysis of the Rh/AZT sample (Fig. S2). However, Rh^{3+} species seem to be notably attenuated after 72 h GDR reaction, suggesting partial reduction of the Rh sites. These results are also in very good agreement with the *in-situ* FTIR findings which will be discussed in the following sections.

It is well known that Ni2p XPS region is rather complex, revealing multiplet-splits and satellites [43,44]. Metallic (Ni^0) species typically yield Ni2p$_{3/2}$ and Ni2p$_{1/2}$ features at 852.7 and 869.9 eV, respectively, in addition to two more satellites at 858.4 and 874.6 eV. NiO (*i.e.* Ni^{2+}) species display multiplet-split for Ni2p$_{3/2}$ and Ni2p$_{1/2}$ signals, leading to four different binding energy (B.E.) values, namely 853.6 and 855.5 eV for Ni2p$_{3/2}$ and 871.9 and 874.0 eV for Ni2p$_{1/2}$. Also, an additional satellite at 879.3 eV also exists for NiO. In contrast, Ni2p$_{3/2}$ and Ni2p$_{1/2}$ signals are located at 855.5 and 874.2 eV for Ni(OH)$_2$, respectively. Ni(OH)$_2$ also exhibits two satellite features at 861.0 eV and 879.3 eV. Based on this knowledge, fresh Ni/AZT catalyst (Fig. 5b) seems to contain predominantly metallic Ni (*i.e.* Ni^0) species with additional contribution from NiO and Ni(OH)$_2$ (*i.e.* Ni^{2+}) species. After 5 h GDR reaction, relative extent of Ni(OH)$_2$ decreases (along with increasing carbon accumulation on the Ni/AZT surface, Table 3). However, after 72 h GDR reaction, Ni(OH)$_2$ species are regenerated due to removal of surface carbon (Table 3) probably through the action of adsorbed H_2O that is produced during GDR reaction.
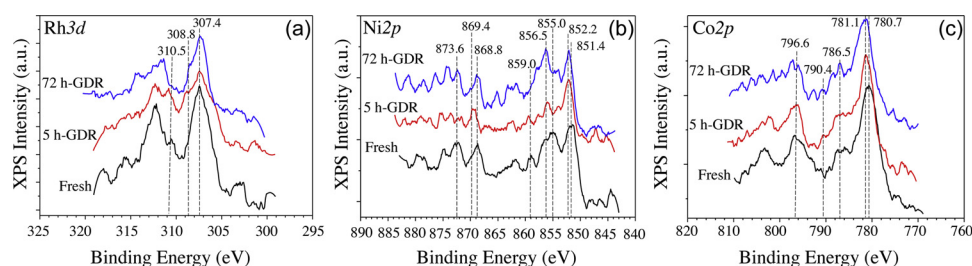

Fig. 5. XPS data for the active sites of fresh (a) Rh/AZT, (b) Ni/AZT, (c) Co/AZT catalysts as well as their spent counterparts used in 5 h and 72 h GDR reaction tests (conditions for spent catalysts: T = 750 °C, CO_2/G = 4, residence time = 3.75 mg$_{cat}$.min/Nml).
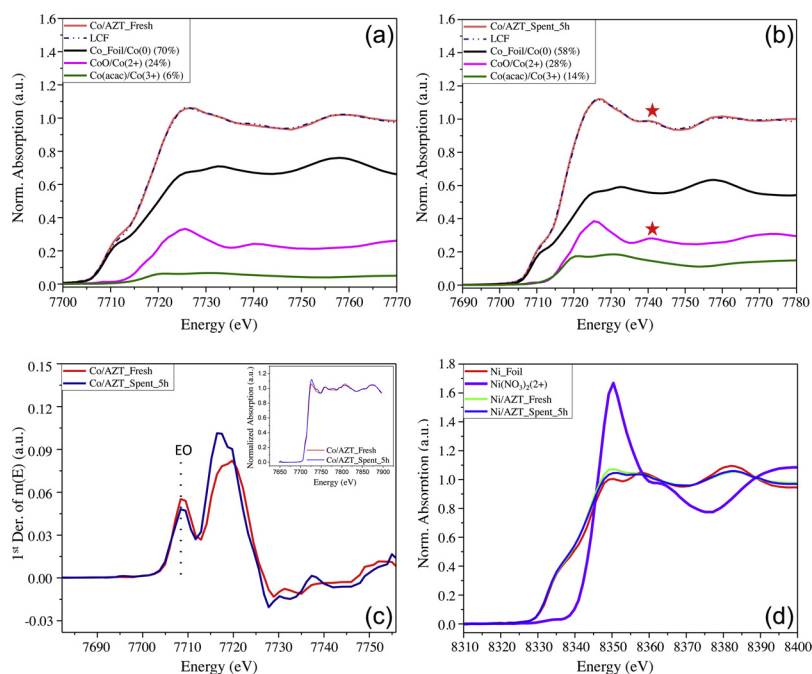
Fig. 6. (a) Co K-edge XANES data for fresh Co/AZT, weighed (70%) Co metal foil, weighed (24%) CoO, weighed (6%) Co(acac)$_3$ and LCF simulation comprised of 70% Co foil, 24% CoO and 6% Co(acac)$_3$, (b) Co K-edge XANES data for 5 h-spent Co/AZT, weighed (58%) Co metal foil, weighed (28%) CoO, weighed (14%) Co(acac)$_3$ and LCF simulation comprised of 58% Co foil, 28% CoO and 14% Co(acac)$_3$, (c) 1st derivative of the Co K-edge XANES spectra for fresh and 5 h-spent Co/AZT (inset shows the corresponding XANES spectra), (d) Ni K-edge XANES data for Ni metal foil, Ni(NO$_3$)$_2$, fresh and 5 h-spent Ni/AZT catalysts (conditions for spent catalysts: T = 750 °C, CO$_2$/G = 4, residence time = 3.75 mg$_{cat}$.min/Nml).

Fig. 5c shows the Co2p region of the XPS data for Co/AZT. Typically, metallic Co^0 species yield a Co2p$_{3/2}$ B.E. of 778.0 eV, while this value shifts to *ca.* 779.8–780.0 eV for CoO (*i.e.* Co^{2+}), Co$_3$O$_4$ (*i.e.* Co^{2+} and Co^{3+}) and Co$_2$O$_3$ (*i.e.* Co^{3+}) and 781.0 eV for Co(OH)$_2$ species [44–48]. Furthermore, Co2p$_{1/2}$ B.E. appears at 795.0 and 795.6 eV for Co$_3$O$_4$ and CoO species, respectively. In addition, CoO species reveal two satellites at 785.7 and 802.5 eV, while these satellites are located at slightly higher B.E. values for Co$_3$O$_4$ (789.6 and 805.0 eV). In the light of this information, it can be argued that convoluted Co2p region of the XPS data for the fresh Co/AZT catalyst contains predominantly CoO (*i.e.* Co^{2+}) species with a smaller contribution from Co$_3$O$_4$, Co$_2$O$_3$ and Co (OH)$_2$. In addition, a miniscule amount of Co^0 species may also be present on the fresh Co/AZT. After 5 h and 72 h GDR reaction tests, changes in the Co2p region of the XPS data is relatively insignificant. On the other hand, a blueshift in the Co2p$_{3/2}$ (B.E.) after 72 h GDR reaction suggest the formation of Co$_3$O$_4$ (*i.e.* Co^{2+} and Co^{3+}) species and partial oxidation of Co sites.

3.1.4. Ex-situ XANES experiments

Fig. 6 shows XANES data obtained for various reference samples such as metallic Co (*i.e.* Co^0) and Ni (*i.e.* Ni^0) foils, CoO (Co^{2+}), Co (C$_5$H$_7$O$_2$)$_3$ (*i.e.* Co^{3+}, Co(acac)$_3$), and Ni(NO$_3$)$_2$ (*i.e.* Ni^{2+}). Furthermore, corresponding XANES data for the fresh and 5 h-spent Co/AZT and Ni/AZT catalysts are also given in Fig. 6. Fig. 6a indicates that the fresh Co/AZT sample is comprised of metallic Co^0 as well as oxidic Co^{2+} and Co^{3+} species [49–51], where relative contributions from these different states can be quantified using a Linear Combination Fitting (LCF) analysis. LCF fit of the fresh Co/AZT sample indicates that relative contributions of different Co oxidation states to the overall Co oxidation state are 70% Co^0, 24% Co^{2+} and 6% Co^{3+} (Table 4). In

contrast to the fresh Co/AZT sample, for the 5 h-spent Co/AZT sample (Fig. 6b and Table 4), Co species seem to be further oxidized as a result of the GDR reaction, leading to a decrease in the contribution from metallic Co species along with an increase in the contributions from Co^{2+} and Co^{3+} oxidic species, revealing contributions of 58% Co^0, 28% Co^{2+} and 14% Co^{3+}. Increase in the oxidic nature of the 5 h-spent Co/ AZT catalyst is also evident by the increase in the shoulder feature depicted with a star in Fig. 6b.

It is worth mentioning that although LCF analysis clearly indicates the oxidation state differences between the fresh and 5 h-spent Co/AZT samples, it is not easy to see significant E$_0$ variations in the Co K-edge spectra of these samples, due to two opposing spectral factors which tend to cancel each other (Fig. 6c). Namely, increase in the contribution of the oxidic species tends to increase E$_0$ values (Fig. 6a and b), while decreasing amount of metallic Co^0 species shifts the E$_0$ values to lower values due to the unique shoulder feature of the metallic Co^0 species located at 7715–7725 eV (Fig. 6a and b). Oxidation of the Co species during the GDR reaction is also in good agreement with the corresponding XPS data given in Fig. 5c revealing catalytic aging and deactivation of Co/AZT systems under GDR reaction conditions.

Ni K-edge XANES data for the fresh and 5 h-spent Ni/AZT systems reveal the presence of mostly Ni^0 species with a smaller contribution from Ni^{2+} species (Fig. 6d) [52,53]. Furthermore, XANES data for the fresh and 5 h-spent Ni/AZT catalysts are quite similar suggesting that Ni active sites can mostly maintain their electronic structures and stability during the 5 h GDR reaction tests. Note that slight decrease in Ni^{2+} (*i.e.* Ni(OH)$_2$) species observed in the current XPS experiments (Fig. 5b) for the 5 h-spent Ni/AZT catalyst can be due to the higher surface sensitivity of the XPS technique, which differs from XANES experiments, where the latter technique has a lower surface sensitivity.

3.1.5. In-situ FTIR spectroscopic experiments

Fig. 7 shows the *in-situ* FTIR spectroscopic characterization of the fresh (*i.e.* reduced) and 72 h-spent (after reaction at 750 °C, CO$_2$/G = 4, residence time = 3.75 mg$_{cat}$.min/Nml) Rh/AZT, Ni/AZT and Co/AZT catalysts. In these experiments, CO(g) was used as a probe molecule in order to shed light on the electronic and morphological properties of the active sites (*i.e.* Rh, Ni and Co) on the catalyst surfaces as well as their interaction with the AZT.

In-situ FTIR spectrum at the bottom of Fig. 7a, corresponds to the

Table 4
Corresponding contributions of Co^0, Co^{2+}, and Co^{3+} species (given in % by weight) in fresh and 5 h-spent Co/AZT samples obtained from current XANES data (conditions for spent catalyst: T = 750 °C, CO$_2$/G = 4, residence time = 3.75 mg$_{cat}$ min/Nml).

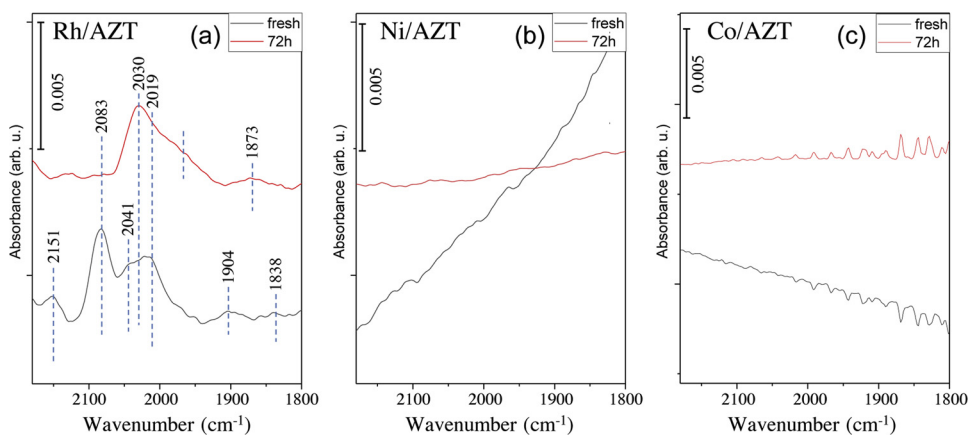|	Co^0	Co^{2+}	Co^{3+}
Co/AZT (fresh)	70	24	6
Co/AZT (5 h-spent)	58	28	14

Fig. 7. *In-situ* FTIR spectra corresponding to 10 Torr CO(g) adsorption at 25 °C for 10 min in the form of fresh and 72 h-spent (a) Rh/AZT, (b) Ni/AZT and (c) Co/AZT catalysts. Before the acquisition of the 72 h-spent catalyst spectra, catalysts were treated with 10 Torr H₂(g) at 300 °C for 10 min followed by evacuation at 25 °C (conditions for spent catalysts: T = 750 °C, CO₂/G = 4, residence time = 3.75 mg_cat.min/Nml).

fresh Rh/AZT catalyst revealing several strong vibrational features associated with different CO(*ads*) species. It is well known that CO can adsorb on Rh⁺ sites *via* the formation of gem-dicarbonyl species (*i.e.* *OC*-Rh⁺−CO or Rh⁺(CO)₂) which are characterized by vibrational features at 2083 and 2019 cm⁻¹ corresponding to the symmetric and anti-symmetric stretchings [29,42,54–58]. Note that multi-carbonyls adsorbed on higher oxidation states of Rh such as tri-carbonyls on Rh³⁺ (Rh³⁺(CO)₃) or tetra carbonyls were not detectable, most likely due to the lower stability of such species at room temperature [57].

Furthermore, IR feature appearing as a shoulder at 2041 cm⁻¹ can be associated with linear (atop) CO(*ads*) on metallic Rh sites. In addition to these, vibrational features located at lower frequencies are spectroscopic finger prints of adsorbed CO species on high-coordination metallic Rh sites. Namely, 1904 and 1838 cm⁻¹ signals can be assigned to CO adsorbed on two-fold (bridging) and three-fold (hollow) metallic Rh⁰ sites, respectively [59–61]. Moreover, vibrational feature at 2151 cm⁻¹ can be ascribed to CO adsorbed on Rh³⁺ sites in a linear (atop) fashion [62] or CO adsorbed on the AZT support or H-bonded adsorbed CO species [63]. These findings suggest that the electronic structure of the exposed Rh sites on the fresh Rh/AZT surface is complicated, revealing co-existence of Rh, Rh⁺ and Rh³⁺ electronic states.

Exposing the Rh/AZT catalyst to GDR reaction conditions for 72 h led to substantial changes in the spectral line shape illustrated in the topmost *in-situ* FTIR spectrum in Fig. 7a. It is clear that the gem-dicarbonyl species on Rh⁺ (Rh⁺(CO)₂) located at 2083 and 2019 cm⁻¹ clearly diminished along with the species located at 2151 cm⁻¹. These observations are in line with the reduction of the Rh³⁺ species to form mainly Rh⁰ species and, to a lesser extent, Rh⁺ species.

As can be seen in Fig. 7b and c, analogous CO(g) adsorption experiments were also carried out *via in-situ* FTIR spectroscopy on fresh, 5 h and 72 h-spent Ni/AZT and Co/AZT catalyst surfaces. However, no significant IR features were detectable for these surfaces. In the case of fresh Ni/AZT and Co/AZT samples, this could be due to the burial/encapsulation of the Ni and Co nanoparticles with the AZT support, preventing CO adsorption at room temperature. It is worth mentioning that very weak CO adsorption features are discernible for the fresh Ni/AZT sample. It is apparent that the initial (fresh) forms of the Ni/AZT

and Co/AZT catalysts experience drastic changes under GDR reaction conditions in order to unveil Ni and Co sites and expose them to reactants. As for the 72 h-spent Ni/AZT and Co/AZT samples, both of these samples seem to be incapable of CO(g) adsorption due to coking. As demonstrated in Section 3.1.3 *via* XPS analysis, even if the coking of 72 h-spent Ni/AZT was significantly lower than that of 72 h-spent Co/AZT, C_s content of 72 h-spent Ni/AZT catalyst was higher than that of its fresh counterpart and this seems to be sufficient to prevent CO(g) adsorption on 72 h-spent Ni/AZT at room temperature.

3.2. Catalytic activity and stability studies

3.2.1. Effect of reaction temperature

Reaction temperature is a key parameter influencing the catalytic activity due to endothermic nature of GDR. Thermal instability of glycerol causes its decomposition under the whole span of the GDR conditions (Section 2.3) in the absence and presence of a catalyst. Therefore, in addition to catalytic experiments, blank tests were performed in an attempt to investigate the extent of homogeneous glycerol conversions to gaseous products. Moreover, a thermodynamic study *via* Gibbs free energy minimization method in CHEMCAD 7.1.4 software was carried out to determine the limits of the reactant conversions at the specified operational conditions. Details of the methodology of thermodynamic analysis can be found elsewhere [29].

Effect of reaction temperature on glycerol conversion to gaseous products over Rh/AZT, Ni/AZT, Co/AZT and blank tests is presented in Fig. 8. It is evident that reaction temperature had a positive effect on catalytic and non-catalytic glycerol conversions, and the difference between thermodynamic limit [29] and the experimental results decreased with increasing temperature. Furthermore, temperature increase promoted catalytic activity and therefore widened the gap between catalytic and non-catalytic glycerol conversions. At 600 °C, there was no significant difference between catalytic and homogeneous glycerol conversions, which were found to range within 7–9% (Fig. 8a). On the other hand, at 750 °C, the highest temperature investigated in the present study, glycerol conversions reached > 80% of the thermodynamic limit in the catalytic experiments. The difference between
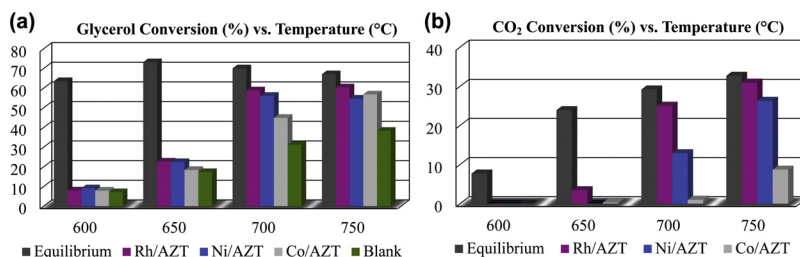

Fig. 8. Effect of reaction temperature on (a) glycerol conversion, (b) CO₂ conversion (CO₂/G = 4, residence time = 0.5 mg_cat.min/Nml).

glycerol conversions obtained on Rh/AZT and in blank tests was ~12% which ramped up to ~58% at 750 °C. There was a significant jump of more than 30% in glycerol conversions when temperature was increased from 650 °C to 700 °C for Rh/AZT and Ni/AZT, whereas this jump remained at 26.5% for Co/AZT. Among the three catalysts, Rh/AZT showed the highest activity at all temperatures.

CO$_2$ conversions with respect to temperature together with the thermodynamic equilibrium limit are given in Fig. 8b. Unlike glycerol, CO$_2$ remained unconverted in the blank tests carried out within the entire operating range. As in the case of glycerol, conversion of CO$_2$ increased significantly with increasing temperature. A discernible increase in thermodynamic CO$_2$ conversion from 7.7% to 23.9% was observed in the 600–650 °C range. A similar change in CO$_2$ conversion (from 3.4% to 25%) was obtained by increasing temperature on Rh/AZT from 650 to 700 °C and the catalyst delivered 86% of the equilibrium conversion at the latter temperature. On the other hand, Ni/AZT and Co/AZT started to demonstrate notable activities at 700 °C and 750 °C, respectively. These findings clearly showed that Rh/AZT outperformed Ni- and Co-based catalysts, and was able to reach up to ~95% of the theoretical limit at 750 °C. Nevertheless, the performance of Ni/AZT at 750 °C should not be overlooked, as it gave 26.3% CO$_2$ conversion, which corresponded to ~80% of its thermodynamic equivalent. At 750 °C, however, Co/AZT remained considerably less active than the Rh- and Ni- based ones, and was able to convert only < 10% of the CO$_2$ fed. Relative activities of the catalysts were in excellent alignment with the differences in the dispersion characteristics and the average size range of the active nanoparticles which were quantified by the detailed TEM-EDX studies explained in the earlier sections. Additional control experiments with the same packing and testing protocols were also carried out by using only the AZT support material to elucidate its intrinsic activity within the studied range of operating conditions. AZT remained inactive between 600–700 °C but gave a very small CO$_2$ conversion of 0.8% at 750 °C (not shown in Fig. 8b). This finding confirmed that the conversions reported in Fig. 8b were dictated by the type of active metal. At 750 °C and CO$_2$/G = 4, glycerol conversion on AZT to gaseous products was found to be 32.3%, which was below the value of 37.6% observed in the blank tests (Fig. 8a). This difference was most likely associated with AZT's catalytic effect which slightly favored RWGS to consume H$_2$ and the reforming routes (Table 1) to convert gaseous C$_1$–C$_2$ hydrocarbons, all of which eventually reduced glycerol conversion *via* Eq. (14).

Product distributions obtained over Rh/AZT, Ni/AZT and Co/AZT are presented in Figs. 9a–c, respectively. Yields of H$_2$ and CO increased with increasing reaction temperature due to elevated conversion of glycerol (Fig. 8a) into H$_2$ and CO (*via* Reaction 2) and C$_1$–C$_2$ hydrocarbons, the latter which were then catalytically reformed by H$_2$O, produced by means of endothermic RGWS promoted at elevated temperatures, and by CO$_2$ into H$_2$ and CO *via* Reactions 4–6 and 7–9, respectively. Yields of CH$_4$, C$_2$H$_4$ and C$_2$H$_6$ increased simultaneously on all catalysts upon increasing the temperature from 600 to 650 °C. This trend was most likely associated with the slight increase in the breakdown of glycerol in the 600–650 °C range and with the reversal of the reforming routes (Table 1) which are exothermic and thermodynamically favored below ~650 °C. The latter argument was in perfect alignment with the fact that steam and dry reforming of methane were not promoted thermodynamically below 620 and 650 °C, respectively [64]. The notable decrease in the C$_1$–C$_2$ yields with temperature > 650 °C confirmed the theoretical predictions of Gao et al. [64] and was associated with the increased extents of hydrocarbon reforming reactions (Table 1). This explanation holds for Rh and Ni, both of which are well known premium catalysts for hydrocarbon reforming to syngas [65]. However, Co/AZT, which was considerably less active than Rh– and Ni–based counterparts, promoted CH$_4$ yield and existence of C$_2$ species with increasing temperature (Fig. 9c). Relative abundance of C$_1$–C$_2$ species on Co/AZT also boosted its glycerol conversion performance (*via* Eq. (14)) and made it closer to those of other catalysts (Fig. 8a). This trend, however, was not observed in case of CO$_2$ conversions (Fig. 8b). Fig. 9d shows the product yields obtained in blank tests. As expected, H$_2$ and CO yields were less than the ones obtained on the catalysts, with the differences becoming significant above 700 °C. Yields of C$_1$–C$_2$ species, however, were at their highest values in the blank experiments. These findings clearly showed that the products of homogeneous glycerol conversion, which increased with temperature (Fig. 9d), stayed in the reaction environment without being post-converted due to the absence of catalytic RWGS and reforming routes.

Syngas compositions (molar H$_2$/CO ratio in the product stream) produced by the catalysts and the blank tests are presented in Fig. 9e. The catalysts followed a common trend that involved maximization of the H$_2$/CO ratio at 700 °C. Increased extents of glycerol breakdown (Reaction 2) and the hydrocarbon steam reforming routes (Reactions 4–6), all of which stoichiometrically deliver more H$_2$ than CO, were the possible drivers of the increase in H$_2$/CO between 650 and 700 °C. This argument agreed well with the decreasing C$_1$–C$_2$ yields on Rh/AZT and Ni/AZT and the reduced rate of increase in the yields of CH$_4$ and C$_2$H$_6$ on Co/AZT in the specified temperature range. The dominance of catalytic RWGS explained the common decrease in H$_2$/CO between 700 and 750 °C over the three catalysts. This explanation was validated by the different H$_2$/CO ratios observed in the non-catalytic experiments
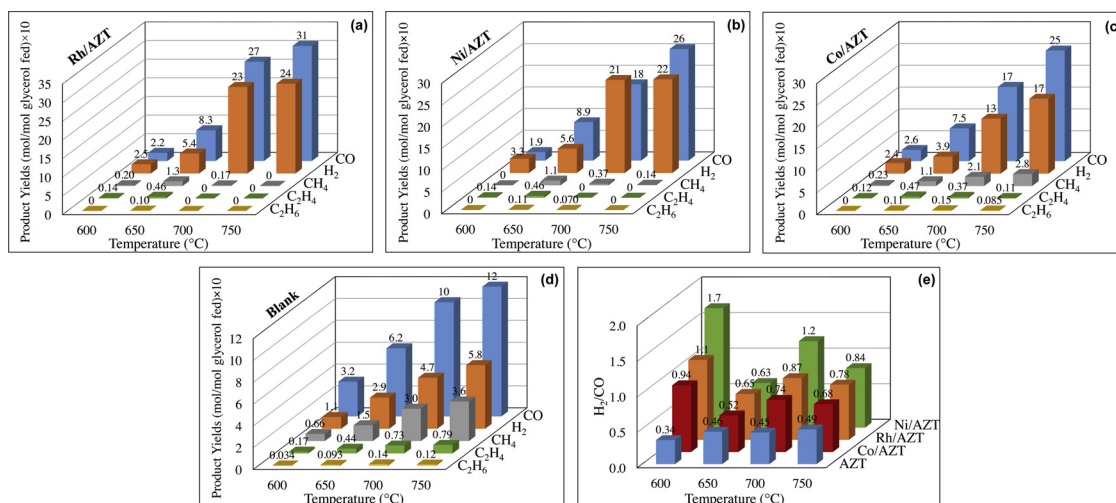

Fig. 9. Effect of reaction temperature on product yields obtained in catalytic (a–c) and blank experiments (d), and on syngas composition (e). (CO$_2$/G = 4, residence time = 0.5 mg$_{cat}$.min/Nml).
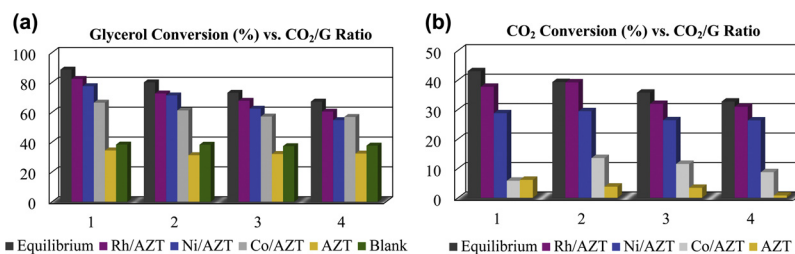
Fig. 10. Effect of CO_2/G on (a) glycerol conversion, (b) CO_2 conversion (T = 750 °C, residence time = 0.5 mg_{cat}.min/Nml).

(Fig. 9e).

The lowest syngas yields and the highest H_2/CO ratios were obtained at 600 °C (Fig. 9e), pointing out faster consumption of CO which was already generated by conversion of glycerol (Fig. 8a). Owing to the facts that formation of C_s species increased progressively with decreasing temperature and was thermodynamically favored below 700 °C under GDR conditions [29], CO consumption at 600 °C could be associated with a series of exothermic coke formation routes, namely the Boudouard reaction (reverse of Reaction 12, Table 1) and with the reverse of Reaction 10 (Table 1) due to relatively limited *in-situ* H_2O production. Thus, it could be revealed that existence of C_s was minimized at 750 °C which was selected as the default temperature in the rest of the experiments. As revealed by the outcomes of current TEM-EDX and XPS analyses, however, C_s species still existed at 750 °C on Co/AZT and - to some extent - Ni/AZT, and affected their stability with magnitudes depending on the catalyst type.

3.2.2. Effect of CO_2/G ratio

Effect of inlet molar CO_2/G ratio is investigated by varying it between 1 and 4, while keeping the temperature and residence time constant at 750 °C and at 0.5 mg_{cat}.min/Nml, respectively. Influence of CO_2/G ratio on glycerol conversion for the catalysts, AZT support and in the blank tests is reported in Fig. 10a together with the corresponding thermodynamic limits. For all catalysts, increasing CO_2/G ratio led to progressive decline in glycerol conversion mainly due to the RWGS (Reaction 3), which was favored by enriching the feed with CO_2. This argument was supported by the lack of a distinct trend in the blank experiments that commonly gave ~38% glycerol conversion at all ratios. Steam, the product of RWGS, is not considered in the definition of glycerol conversion to gaseous products (Eq. (14)). Impact of the lack of H_2O in Eq. (14) was analyzed and reported to be negligible in [29]. Fig. 10a also showed that Rh/AZT was the most active catalyst that gave the highest conversion of 82.3% at CO_2/G = 1. Glycerol conversions above 90% of the pertinent theoretical limits were achieved on Rh/AZT at all of the currently used CO_2/G ratios. Ni/AZT and Co/AZT, on the other hand, only delivered ~80% and ~75% of the equilibrium limit, respectively.

The effect of CO_2/G ratio on CO_2 conversions and on product distributions are shown in Figs. 10b and 11 a–f, respectively. The catalysts showed increase in activity upon increasing CO_2/G from 1 to 2, above which CO_2 conversions decreased (Fig. 10b). Similarly, Siew et al. [17,19] reported that the activity of their Ni–based catalysts first increased upon changing CO_2/G ratio from 0 to 1.68 and then decreased. Improved GDR activity of Ni and noble metal catalysts by increasing CO_2/G ratio from 0 to 3 was also reported [27,28]. Among the currently investigated catalysts, Rh/AZT clearly gave the highest CO_2 conversions in the complete span of the feed composition and remained highly active to deliver near equilibrium conversions. On the other hand, Ni/AZT was found to give CO_2 conversions that were much less sensitive to the feed ratio than the ones obtained on Rh/AZT. Decrease in CO_2 conversion upon increasing CO_2/G from 2 to 4 was calculated as 9.9%, 21.1% and 35.6% for Ni, Rh and Co, respectively (Fig. 10b). This order was correlated with the H_2/CO ratios that were found to be the highest on Ni and lowest on Co at all feed ratios (Fig. 11f). In other words,

maximum promotion of H_2–rich production was detected on Ni/AZT. Considering the fact that Ni is well–known for its high WGS activity under reforming conditions [65], it can be claimed that Reaction 3 was suppressed by its reverse to produce H_2 and CO_2, where the latter reduced the dependence of CO_2 conversion on CO_2/G on Ni/AZT.

Product distributions obtained on all catalysts (Fig. 11a–c) followed a common and distinct pattern that involved monotonic decrease and increase in H_2 and CO yields, respectively, by increasing CO_2/G. These findings clearly indicated the impact of RWGS on catalytic responses. Catalytic nature of this reaction was also evident in Fig. 11d which showed that the yields responded to changes in CO_2/G in a notably different pattern in the absence of a catalyst. Furthermore, detection of $Co(OH)_2$ and $Ni(OH)_2$ in the current XPS experiments (Fig. 5) also supported the direct modification of the catalyst surface chemistry due to the production of H_2O, a product of RWGS, under GDR conditions. As a result of *in-situ* H_2O generation, CH_4, C_2H_4 and C_2H_6 were consumed mainly by the catalytic steam reforming routes (Reactions 4–6, Table 1) which were kinetically and thermodynamically favored at the pertinent operating conditions. This argument was supported by the almost negligible/non-existing yields of C_1–C_2 species, whose extents of consumption followed the order of activity, namely Rh > Ni > Co.

Current TEM-EDX imaging together with XPS analyses indicated existence of C_s species at 750 °C. Considering that the characterization studies were carried out at CO_2/G = 4, increase in the amount of C_s could be expected at lower CO_2/G ratios due to reverse of Reaction 10–12 (Table 1) that were favored at reduced amounts of CO_2 in the feed and H_2O in the reaction medium, the latter being caused by suppression of RWGS. The opposite of this argument can be used to explain the increase in CO_2 conversion upon changing CO_2/G from 1 to 2 on all catalysts (Fig. 10b). In other words, promotion of Reactions 10–12 (Table 1) could gasify C_s species and increase the activity of the catalysts. This statement was supported by the per cent change in the yield of CO (the primary product of gasification reactions) which reached to its maximum value (12%, 9.1% and 15% on Rh, Ni and Co, respectively) between CO_2/G of 1 and 2 (Fig. 11a–c). Decreasing CO_2 conversions at CO_2/G > 2 could be attributed to Reaction 11 which was favored to convert C_s into CO_2 among other gasification routes (Reactions 10 and 12) due to its lower enthalpy and presence of H_2O in the reaction medium.

Fig. 10b presents the role of AZT on CO_2 conversion. Interestingly, AZT showed some activity towards CO_2, which decreased by increasing CO_2/G ratio and almost faded out at CO_2/G = 4. Comparison of Fig. 11d and e showed that yields of H_2 and CO were higher than their counterparts measured in the blank experiments, and the contribution of AZT to CO formation was more notable than its impact on H_2 production. These trends pointed out possible roles of AZT in converting C_s species *via* Reactions 10–12 (Table 1) and promoting Reaction 3. As explained in detail in one of our former reports [66], AZT is a complex mixed oxide. It lacks a well-defined XRD pattern, exhibits a quite disordered surface structure, and hosts a large number of various crystal defects such as oxygen vacancies, heterojunctions and interfacial sites, between various oxide domains. Hence, it is likely that owing to its heterogeneous composition and complex surface chemistry, AZT may be able to convert C_s into CO. In addition to these routes, AZT seemed to
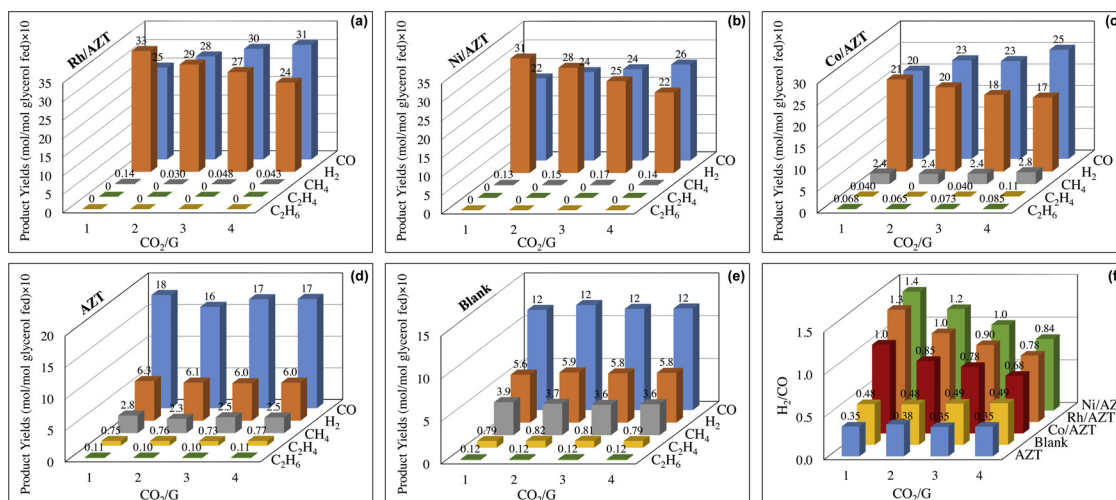
Fig. 11. Effect of CO_2/G ratio on product yields obtained in catalytic (a–c) and blank experiments (d–e), and on syngas composition (f). (T = 750 °C, residence time = 0.5 mg_{cat}.min/Nml).
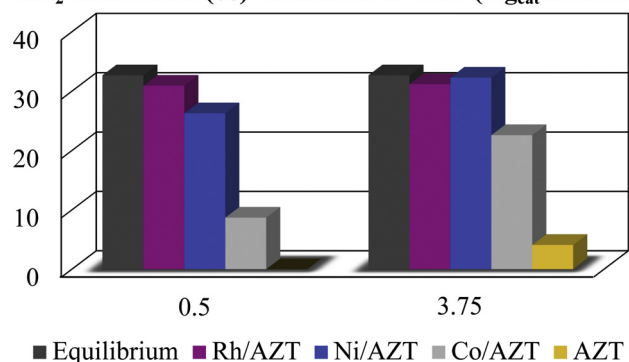

Fig. 12. CO_2 conversions obtained as a function of residence time (T = 750 °C, CO_2/G = 4).

contribute to Reactions 7–9, which, compared to those obtained in blank tests, led to reduced yields of CH_4, C_2H_4 and C_2H_6 and increased yields of H_2 and CO.

3.2.3. Effect of residence time

The effect of residence time on CO_2 conversions of the investigated catalysts, AZT support and the blank tests are presented in Fig. 12. Rh/AZT gave the lowest response (i.e. < 1% increase in CO_2 conversion) to the increase in residence time from 0.5 to 3.75 mg_{cat}.min/Nml. In other words, Rh/AZT was capable of delivering more than 95% of the equilibrium CO_2 conversion of 32.7% even at the shortest residence time that corresponded to a catalyst amount of 20 mg. This finding was a clear indication of superior activity of Rh/AZT which was fundamentally based on its resistance against carbon formation, fine dispersion of Rh nanoparticles and the small average Rh particle size range of 3–4 nm. The number of available active sites in 20 mg of Rh/AZT were sufficient to deliver near–equilibrium CO_2 conversion. Therefore, further increase in the amount of Rh/AZT led to negligible improvement in the activity. Fig. 12 also showed that the gap between CO_2 conversions obtained at different residence times increased with decreasing catalytic activity and reached to a maximum of 13.6% on Co/AZT on which Co nanoparticles are poorly dispersed with average size range of 40–50 nm on the AZT surface.

Interestingly, when run at 3.75 mg_{cat}.min/Nml Ni/AZT catalyzed GDR almost at the thermodynamic limit (Fig. 12). Therefore, a more detailed investigation on residence time effect over Ni/AZT was carried out. For this purpose, 50 and 100 mg of Ni/AZT that corresponded to

residence times of 1.25 and 2.5 mg_{cat}.min/Nml, respectively were tested additionally at default operating conditions of 750 °C and CO_2/G = 4 (data shown in Fig. 12 only for 0.5 and 3.75 mg_{cat}.min/Nml). Increasing the amount of Ni/AZT from 20 to 50 mg elevated CO_2 conversion from 26.3% to 31.2%, whereas further increase to 150 mg changed conversion from 31.2% only to 32.3%, which was very close to the equilibrium value of 32.7%. Therefore, in addition to Rh/AZT, Ni/AZT can also be classified as a highly active catalyst as only 50 mg of it was sufficient to deliver 95% of the equilibrium conversion. Besides being highly active, Rh/AZT and Ni/AZT were also shown to be stable as discussed in the following section. Finally, testing of the AZT support material at longer residence times gave CO_2 conversions up to 4.1%. Possible reactive routes on AZT were discussed in Section 3.2.2.

3.2.4. Catalyst stability

Stability of the Rh/AZT, Ni/AZT and Co/AZT catalysts are investigated in the context of 72 h TOS experiments carried out at 750 °C and CO_2/G = 4. Residence time is kept at its highest value (3.75 mg_{cat}.min/Nml) to magnify the impacts of possible deactivation scenarios on the catalysts via their increased interaction with the reactive mixture. The results, expressed in terms of CO_2 conversions with respect to time, are presented in Fig. 13. In the course of their 72 h TOS tests, both Rh/AZT and Ni/AZT demonstrated CO_2 conversions above > 91% of the thermodynamic limit and remained in their active states with only less than 13% and 8% decrease in CO_2 conversions, respectively. In order to interpret these findings which are thought to be related with the support material, CO_2 conversions obtained on ZrO_2 and CeO_2 supported 1% Rh loaded catalysts previously [29] by their 72 h TOS testing under the same operating conditions are shown in Fig. 13. The results clearly showed that Rh/AZT was more active and stable than Rh/ZrO_2 and Rh/CeO_2, which showed 40% and 23%
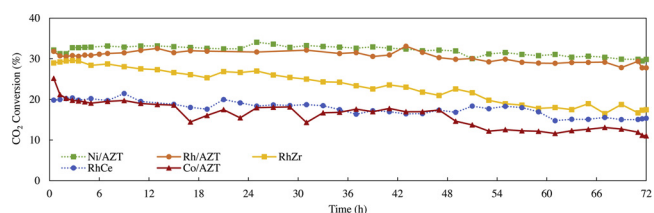

Fig. 13. CO_2 conversions obtained in the stability tests carried out for 72 h (T = 750 °C, CO_2/G = 4, residence time = 3.75 mg_{cat}.min/Nml). Time-on-stream data for the Rh/ZrO_2 (RhZr) and Rh/CeO_2 (RhCe) catalysts are adapted from [29].

decrease in CO_2 conversions, respectively at the end of 72 h. Spectroscopic evidence reported in [29] showed that deactivation of Rh/ZrO$_2$ was driven by hydrothermal sintering and formation of C$_s$ species, both of which were reduced on CeO$_2$ by strong metal-support interaction effects. These comparisons pointed out that AZT possibly aided in reducing the extents of surface migration of Rh nanoparticles and formation of surface carbon species, both of which were in accordance with the findings of the current structural and function characterization studies explained in Section 3.1. Ni, a much cheaper alternative of Rh, was shown to be a very active and stable catalyst that almost preserved its original metallic nature and dispersion pattern, and gasified the carbonaceous species deposited within the first few hours of the experiments (Table 3). Fig. 13 also illustrated severe deactivation of Co/AZT, which was obvious by > 50% decrease in CO_2 conversion from 25.2% to 11.0%. As explained earlier, activity loss of Co/AZT was driven by notable sintering, monotonic accumulation of carbonaceous deposits and oxidation of the Co sites. Despite its relatively fast deactivation, however, Co/AZT delivered conversions comparable to those obtained on Rh/CeO$_2$ until 47th h of the TOS test. This finding could be another indication of the impact of support material that can make Co, a relatively inactive metal for reforming reactions, comparable with Rh.

As formulated in Eq. (13), CO_2 conversion could be calculated directly from its inlet and exit flow rates, both of which were known precisely by means of accurate dosing and product analysis equipment. It was also obvious that breakdown of CO_2 occurred only in the presence of a catalyst (Fig. 10b). Therefore, the use of CO_2 conversion provided correct insight into understanding the lifetime of the pertinent catalyst used under GDR conditions. Interestingly, the limited number of GDR studies involving 72 h longevity tests in the literature [17,23] involved glycerol conversion as the only metric to describe catalyst deactivation. In other words, the literature lacks benchmarks for the results reported in Fig. 13. However, its notable consumption in homogeneous reactions make the conversion of glycerol an improper indicator of the catalytic activity. Despite the ambiguities in its use to quantify catalyst stability, glycerol conversion changed only by < 2% on the AZT supported catalysts at the end of 72 h TOS experiments (data not presented). On the other hand, at the end of 72 h TOS testing of 3% La-20% Ni/Al$_2$O$_3$ and 20% Ni/CC catalysts, glycerol conversion decreased by ~25% and more than 50%, respectively [17,23]. In this respect, AZT supported catalysts clearly outperform their counterparts reported in the literature.

4. Conclusions

Glycerol dry reforming (GDR) to syngas was studied on Al$_2$O$_3$-ZrO$_2$-TiO$_2$ (AZT) supported Rh, Ni and Co–based catalysts in a series of activity tests carried out at 600–750 °C, CO_2/G = 1–4 and residence time = 0.5–3.75 mg$_{cat}$.min/Nml. In order to provide fundamental insight into their characteristic roles in GDR, catalysts used for 5 h and 72 h under reactive environment are characterized comparatively with their fresh (*i.e.* reduced) counterparts by means of detailed molecular-level *in-situ/ex-situ* spectroscopic/imaging techniques such as TEM-EDX, XPS, XANES and *in-situ* FTIR. The key findings can be summarized as follows:

- Glycerol and CO_2 conversions decreased in the following order: 1% Rh/AZT > 5% Ni/AZT > 5% Co/AZT, which was well correlated with the average particle sizes of corresponding active metal nanoparticles (3–4, 10–15 and 40–50 nm for Rh, Ni and Co, respectively). Due to their exceptional activity and stability, Rh/AZT and its cheaper alternative, Ni/AZT significantly outperformed their counterparts in the literature and delivered stable production of syngas at H$_2$/CO = 0.75–0.9 (close to the ideal value of ~1) with CO_2 and glycerol conversions above 30% and 60%, i.e. > ~90% of their theoretical limits, respectively.
- Rh/AZT gave CO_2 and glycerol conversions above 90% of their

thermodynamic equivalents even at the shortest residence time of 0.5 mg$_{cat}$.min/Nml, and remained stable due to the lack of sintering and deposition of surface carbon species.
- While its activity was below that of Rh/AZT at the residence time of 0.5 mg$_{cat}$.min/Nml, Ni/AZT became capable of delivering ~95% of the thermodynamic CO_2 conversion upon its elongated contact (> 1.25 mg$_{cat}$.min/Nml) with the reactive stream. Remarkable activity and stability of Ni/AZT were attributed to its ability of post-gasifying surface carbon species deposited initially (*i.e.* in the first few hours) of reaction tests and to its metallic nature together with dispersion pattern both of which remained almost unchanged.
- Activity and stability of Co/AZT, however, were significantly below those of Rh and Ni due to superposition of clustering and oxidation of Co sites, and severe carbon formation that was irreversible. Nevertheless, similar performances of Co/AZT and Rh/CeO$_2$, tested previously in [29], highlighted the impact of AZT support which seemed to contribute to mechanisms of RGWS, surface carbon gasification and C$_1$-C$_2$ steam/CO_2 reforming.

Declaration of interest

None.

Appendix A. Supplementary data

Supplementary material related to this article can be found, in the online version, at doi:https://doi.org/10.1016/j.apcatb.2019.117808.

References

[1] U.S. Energy Information Administration, Annual Energy Outlook 2015 with Projections to 2040, (2015) (Accessed 5 February 2019), https://www.eia.gov/outlooks/aeo/pdf/0383(2015).pdf.
[2] UFOP, UFOP Report on Global Market Supply, (2018) (Accessed 11 February 2019), https://www.ufop.de/files/3515/1515/2657/UFOP_Report_on_Global_Market_Supply_2017-2018.pdf.
[3] National Biodiesel Board, Biodiesel Basics, (2016) (Accessed 14 February 2019), https://biodiesel.org/what-is-biodiesel/biodiesel-basics.
[4] U.S. Energy Information Administration, Monthly Biodiesel Production Report with Data for April 2018, (2018) (Accessed 5 February 2019), https://www.eia.gov/biofuels/biodiesel/production/.
[5] Y.-C. Lin, Catalytic valorization of glycerol to hydrogen and syngas, Int. J. Hydrogen Energy 38 (2013) 2678–2700.
[6] C.A. Schwengber, H.J. Alves, R.A. Schaffner, F.A. da Silva, R. Sequinel, V.R. Bach, R.J. Ferracin, Overview of glycerol reforming for hydrogen production, Renew. Sustain. Energy Rev. 58 (2016) 259–266.
[7] A. Delparish, A.K. Avci, Intensified catalytic reactors for Fischer-Tropsch synthesis and for reforming of renewable fuels to hydrogen and synthesis gas, Fuel Process. Technol. 151 (2016) 72–100.
[8] A. Delparish, A.K. Avci, Modeling of intensified glycerol steam reforming in a heat-exchange integrated microchannel reactor, Catal. Today 299 (2018) 328–338.
[9] J.M. Silva, M.A. Soria, L.M. Madeira, Challenges and strategies for optimization of glycerol steam reforming process, Renew. Sustain. Energy Rev. 42 (2015) 1187–1213.
[10] N. Abatzoglou, C. Fauteux-Lefebvre, Review of catalytic syngas production through steam or dry reforming and partial oxidation of studied liquid compounds, Wiley Interdiscip. Rev.: Energy Environ. 5 (2016) 169–187.
[11] D. Pakhare, J. Spivey, A review of dry (CO2) reforming of methane over noble metal catalysts, Chem. Soc. Rev. 43 (2014) 7813–7837.
[12] A. de Klerk, Fischer-Tropsch Refining, Wiley-VCH, Weinheim, 2011.
[13] A.C.D. Freitas, R. Guirardello, Comparison of several glycerol reforming methods for hydrogen and syngas production using Gibbs energy minimization, Int. J.

Hydrogen Energy 39 (2014) 17969–17984.

[14] G.R. Kale, B.D. Kulkarni, Thermodynamic analysis of dry autothermal reforming of glycerol, Fuel Process. Technol. 91 (2010) 520–530.

[15] X. Wang, M. Li, M. Wang, H. Wang, S. Li, S. Wang, X. Ma, Thermodynamic analysis of glycerol dry reforming for hydrogen and synthesis gas production, Fuel 88 (2009) 2148–2153.

[16] T. Valliyappan, N.N. Bakhshi, A.K. Dalai, Pyrolysis of glycerol for the production of hydrogen or syn gas, Bioresour. Technol. 99 (2008) 4476–4483.

[17] K.W. Siew, H.C. Lee, J. Gimbun, S.Y. Chin, M.R. Khan, Y.H. Taufiq-Yap, C.K. Cheng, Syngas production from glycerol-dry(CO_2) reforming over La-promoted Ni/Al_2O_3 catalyst, Renew. Energy 74 (2015) 441–447.

[18] K.W. Siew, H.C. Lee, M.R. Khan, J. Gimbun, C.K. Cheng, CO_2 reforming of glycerol over La-Ni/Al_2O_3 catalyst: a longevity evaluative study, J. Energy Chem. 24 (2015) 366–373.

[19] K.W. Siew, H.C. Lee, J. Gimbun, C.K. Cheng, Production of CO-rich hydrogen gas from glycerol dry reforming over La-promoted Ni/Al_2O_3 catalyst, Int. J. Hydrogen Energy 39 (2014) 6927–6936.

[20] K.W. Siew, H.C. Lee, J. Gimbun, C.K. Cheng, Characterization of La-promoted Ni/Al_2O_3 catalysts for hydrogen production from glycerol dry reforming, J. Energy Chem. 23 (2014) 15–21.

[21] N. Harun, J. Gimbun, M.T. Azizan, S.Z. Abidin, Characterization of Ag-promoted Ni/SiO_2 catalysts for syngas production via carbon dioxide (CO_2) dry reforming of glycerol, Bull. Chem. React. Eng. Catal. 11 (2016) 220–229.

[22] N. Harun, S.Z. Abidin, O.U. Osazuwa, Y.H. Taufiq-Yap, M.T. Azizan, Hydrogen production from glycerol dry reforming over Ag-promoted Ni/Al_2O_3, Int. J. Hydrogen Energy (2018).

[23] H.C. Lee, K.W. Siew, J. Gimbun, C.K. Cheng, Synthesis and characterisation of cement clinker-supported nickel catalyst for glycerol dry reforming, Chem. Eng. J. 255 (2014) 245–256.

[24] H.C. Lee, K.W. Siew, M.R. Khan, S.Y. Chin, J. Gimbun, C.K. Cheng, Catalytic performance of cement clinker supported nickel catalyst in glycerol dry reforming, J. Energy Chem. 23 (2014) 645–656.

[25] N.N. Mohd Arif, N. Harun, N.M. Yunus, D.-V.N. Vo, M.T. Azizan, S. Zainal Abidin, Reforming of glycerol for hydrogen production over Ni based catalysts: effect of support type, Energy Sources Part A 39 (2017) 657–663.

[26] N.N. Mohd Arif, D.-V.N. Vo, M.T. Azizan, S.Z. Abidin, Carbon dioxide dry reforming of glycerol for hydrogen production using Ni/ZrO_2 and Ni/CaO as catalysts, Bull. Chem. React. Eng. Catal. 11 (2016) 200–209.

[27] M. Tavanarad, F. Meshkani, M. Rezaei, Production of syngas via glycerol dry reforming on Ni catalysts supported on mesoporous nanocrystalline Al_2O_3, J. CO_2 Util. 24 (2018) 298–305.

[28] M. Tavanarad, F. Meshkani, M. Rezaei, Synthesis and application of noble metal nanocatalysts supported on $MgAl_2O_4$ in glycerol dry reforming reaction, Catal. Lett. 148 (2018) 164–172.

[29] P.S. Bulutoglu, Z. Say, S. Bac, E. Ozensoy, A.K. Avci, Dry reforming of glycerol over Rh-based ceria and zirconia catalysts: new insights on catalyst activity and stability, Appl. Catal., A 564 (2018) 157–171.

[30] Z. Say, M. Tohumeken, E. Ozensoy, NO_x storage and reduction pathways on zirconia and titania functionalized binary and ternary oxides as NO_x storage and reduction (NSR) systems, Catal. Today 231 (2014) 135–144.

[31] A.I. Tsyganok, M. Inaba, T. Tsunoda, S. Hamakawa, K. Suzuki, T. Hayakawa, Dry reforming of methane over supported noble metals: a novel approach to preparing catalysts, Catal. Commun. 4 (2003) 493–498.

[32] Z. Hou, T. Yashima, Small amounts of Rh-promoted Ni catalysts for methane reforming with CO_2, Catal. Lett. 89 (2003) 193–197.

[33] A.M. da Silva, K.R. de Souza, G. Jacobs, U.M. Graham, B.H. Davis, L.V. Mattos, F.B. Noronha, Steam and CO_2 reforming of ethanol over Rh/CeO_2 catalyst, Appl. Catal., B 102 (2011) 94–109.

[34] A. Drif, N. Bion, R. Brahmi, S. Ojala, L. Pirault-Roy, E. Turpeinen, P.K. Seelam, R.L. Keiski, F. Epron, Study of the dry reforming of methane and ethanol using Rh catalysts supported on doped alumina, Appl. Catal. A 504 (2015) 576–584.

[35] K.J. Puolakka, S. Juutilainen, A.O.I. Krause, Combined CO_2 reforming and partial oxidation of n-heptane on noble metal zirconia catalysts, Catal. Today 115 (2006) 217–221.

[36] J.G. Jakobsen, M. Jakobsen, I. Chorkendorff, J. Sehested, Methane steam reforming kinetics for a rhodium-based catalyst, Catal. Lett. 140 (2010) 90–97.

[37] S. Koc, A.K. Avci, Reforming of glycerol to hydrogen over Ni-based catalysts in a microchannel reactor, Fuel Process. Technol. 156 (2017) 357–365.

[38] E. Kayhan, S.M. Andonova, G.S. Şentürk, C.C. Chusuei, E. Ozensoy, Fe promoted NO_x storage materials: structural properties and NO_x uptake, J. Phys. Chem. C 114 (2010) 357–369.

[39] P. Basu, T.H. Ballinger, J.T. Yates, Wide temperature range IR spectroscopy cell for studies of adsorption and desorption on high area solids, Rev. Sci. Instrum. 59

(1988) 1321–1327.

[40] B. Ravel, M. Newville, ATHENA, ARTEMIS, HEPHAESTUS: data analysis for X-ray absorption spectroscopy using IFEFFIT, J. Synchrotron Radiat. 12 (2005) 537–541.

[41] A. Kaniyoor, T.T. Baby, T. Arockiadoss, N. Rajalakshmi, S. Ramaprabhu, Wrinkled graphenes: a study on the effects of synthesis parameters on exfoliation-reduction of graphite oxide, J. Phys. Chem. C 115 (2011) 17660–17669.

[42] D.I. Kondarides, Z. Zhang, X.E. Verykios, Chlorine-induced alterations in oxidation state and CO chemisorptive properties of CeO_2-supported Rh catalysts, J. Catal. 176 (1998) 536–544.

[43] K.S. Kim, N. Winograd, X-ray photoelectron spectroscopic studies of nickel-oxygen surfaces using oxygen and argon ion-bombardment, Surf. Sci. 43 (1974) 625–643.

[44] N.S. McIntyre, M.G. Cook, X-ray photoelectron studies on some oxides and hydroxides of cobalt, nickel, and copper, Anal. Chem. 47 (1975) 2208–2213.

[45] C.V. Schenck, J.G. Dillard, J.W. Murray, Surface analysis and the adsorption of Co (II) on goethite, J. Colloid Interface Sci. 95 (1983) 398–409.

[46] R. Dedryvère, S. Laruelle, S. Grugeon, P. Poizot, D. Gonbeau, J.M. Tarascon, Contribution of X-ray photoelectron spectroscopy to the study of the electro-chemical reactivity of CoO toward lithium, Chem. Mater. 16 (2004) 1056–1061.

[47] J. Yang, H. Liu, W.N. Martens, R.L. Frost, Synthesis and characterization of cobalt hydroxide, cobalt oxyhydroxide, and cobalt oxide nanodiscs, J. Phys. Chem. C 114 (2010) 111–119.

[48] V.M. Jiménez, A. Fernández, J.P. Espinós, A.R. González-Elipe, The state of the oxygen at the surface of polycrystalline cobalt oxide, J. Electron. Spectrosc. Relat. Phenom. 71 (1995) 61–71.

[49] H. Liang, Y. Hong, C. Zhu, S. Li, Y. Chen, Z. Liu, D. Ye, Influence of partial Mn-substitution on surface oxygen species of $LaCoO_3$ catalysts, Catal. Today 201 (2013) 98–102.

[50] O. Haas, F. Holzer, S. Müller, J.M. McBreen, X.Q. Yang, X. Sun, M. Balasubramanian, X-ray absorption and diffraction studies of $La_{0.6}Ca_{0.4}CoO_3$ perovskite, a catalyst for bifunctional oxygen electrodes, Electrochim. Acta 47 (2002) 3211–3217.

[51] O. Haas, R.P.W.J. Struis, J.M. McBreen, Synchrotron X-ray absorption of $LaCoO_3$ perovskite, J. Solid State Chem. 177 (2004) 1000–1010.

[52] W.E. O'Grady, K.I. Pandya, K.E. Swider, D.A. Corrigan, In situ X-ray absorption near-edge structure evidence for quadrivalent nickel in nickel battery electrodes, J. Electrochem. Soc. 143 (1996) 1613–1617.

[53] R.J. Woolley, B.N. Illy, M.P. Ryan, S.J. Skinner, In situ determination of the nickel oxidation state in $La_2NiO_{4+δ}$ and $La_4Ni_3O_{10-δ}$ using X-ray absorption near-edge structure, J. Mater. Chem. 21 (2011) 18592–18596.

[54] C.A. Rice, S.D. Worley, C.W. Curtis, J.A. Guin, A.R. Tarrer, The oxidation state of dispersed Rh on Al_2O_3, J. Chem. Phys. 74 (1981) 6487–6497.

[55] S.S.C. Chuang, S. Debnath, Infrared study of the formation of Rh^+ $(CO)_2$ over $RhCl_3$/SiO_2 and its reactivity with NO, J. Mol. Catal. 79 (1993) 323–334.

[56] J.A. Anderson, C.H. Rochester, Infrared study of CO adsorption on Pt–Rh/Al_2O_3 catalysts, J. Chem. Soc. Faraday Trans. 87 (1991) 1479–1483.

[57] E. Ivanova, K. Hadjiivanov, Polycarbonyls of Rh^+ formed after interaction of CO with Rh–MFI: an FTIR spectroscopic study, PCCP 5 (2003) 655–661.

[58] M.I. Zaki, B. Tesche, L. Kraus, H. Knözinger, Supported rhodium catalysts. Support effects on state and dispersion of the rhodium, Surf. Interface Anal. 12 (1988) 239–246.

[59] C.D. Zeinalipour-Yazdi, A.L. Cooksy, A.M. Efstathiou, A diffuse reflectance infrared Fourier-transform spectra and density functional theory study of CO adsorption on Rh/γ-Al_2O_3, J. Phys. Chem. C 111 (2007) 13872–13878.

[60] M.M.M. Jansen, B.E. Nieuwenhuys, D.C. Ferré, J.W. Niemantsverdriet, Influence of nitrogen atoms on the adsorption of CO on a Rh(100) single crystal surface, J. Phys. Chem. C 113 (2009) 12277–12285.

[61] G. Krenn, I. Bako, R. Schennach, CO adsorption and CO and O coadsorption on Rh (111) studied by reflection absorption infrared spectroscopy and density functional theory, J. Chem. Phys. 124 (2006) 144703.

[62] K. Hadjiivanov, E. Ivanova, L. Dimitrov, H. Knözinger, FTIR spectroscopic study of CO adsorption on Rh–ZSM-5: detection of Rh^+–CO species, J. Mol. Struct. 661–662 (2003) 459–463.

[63] M.P. Seah, The quantitative analysis of surfaces by XPS: a review, Surf. Interface Anal. 2 (1980) 222–239.

[64] J. Gao, Z. Hou, H. Lou, X. Zheng, Dry (CO_2) reforming, in: D. Shekhawat, J.J. Spivey, D.A. Berry (Eds.), Fuel Cells: Technologies for Fuel Processing, Elsevier, Amsterdam, 2011, pp. 191–221.

[65] Z.I. Onsan, A.K. Avci, Multiphase Catalytic Reactors: Theory, Design, Manufacturing, and Applications, Wiley, Hoboken, New Jersey, 2016.

[66] Z. Say, O. Mihai, M. Tohumeken, K.E. Ercan, L. Olsson, E. Ozensoy, Sulfur-tolerant BaO/ZrO_2/TiO_2/Al_2O_3 quaternary mixed oxides for deNO_x catalysis, Catal. Sci. Technol. 7 (2017) 133–144.